RSC Advances

PAPER

View Article Online
View Journal | View Issue

Cite this: *RSC Adv.*, 2026, **16**, 21867

Novel piperazine–triazole hybrids as PTP1B and alpha-amylase inhibitors: synthesis, biological evaluation and computational validation through network pharmacology, molecular docking, MD simulations, DFT and MMPBSA analysis

Muhammad Haroon,[a] Shagufta Kamal,[b] Asim Mansha[a] and Ameer Fawad Zahoor *[a]

The inhibition of α-amylase and PTP1B is essential for controlling hyperglycemia and improving insulin signaling. In this study, a series of piperazine conjugates were synthesized in 61–78% yields. All compounds were biologically screened against α-amylase to assess their anti-diabetic potential. Among these, compounds with Cl and OMe substitutions showed exceptional enzyme inhibition with IC_{50} values of 2.39 ± 0.41 μM and 2.97 ± 0.31 μM, respectively, higher than standard acarbose (10.30 ± 0.20 μM). Further network pharmacology study was conducted, which spotted PTP1B as an important target to improve insulin signaling. Molecular docking analysis of potent compounds was performed to evaluate interactions of inhibitors with target receptors (PTP1B & α-amylase). Both compounds validated the *in vitro* protocols by showing excellent binding affinities −10.5 kcal mol^{-1} and −9.7 kcal mol^{-1} against α-amylase, surpassing standard acarbose (−8.1 kcal mol^{-1}). Likewise, both of them exhibited a similar binding pattern with binding affinities of −8.0 kcal mol^{-1} & −7.8 kcal mol^{-1} against PTP1B, even better than the reference acarbose (−7.4 kcal mol^{-1}). DFT studies were carried out to determine electronic properties, which were corroborated through NCI analysis. Furthermore, 500 ns MD simulation, binding free energy calculations, PCA, DCCM and FEL analysis were carried out to evaluate thermodynamic stability.

Received 3rd February 2026
Accepted 27th March 2026

DOI: 10.1039/d6ra00931j

rsc.li/rsc-advances

1 Introduction

The WHO (World Health Organization) has identified noninfectious disorders such as obesity and diabetes mellitus as major causes of worldwide health crises.[1,2] Diabetes mellitus refers to persistent metabolic disease marked by elevated blood glucose (hyperglycemia) stemming from inadequate insulin secretion.[3–7] According to the IDF (International Diabetes Federation), this disease has affected more than 463 million people worldwide, which is predicted to rise to 578 million in the next five years.[8,9] This situation amplifies the threat of critical issues such as retinopathy,[10] heart failure,[11] strokes[12] and nephropathy.[13] Diabetes can be managed by controlling the blood glucose level through the suppression of carbohydrate-degrading enzymes such as α-amylase.[14–17] The α-amylase breaks down the starch into smaller subunits such as maltose and glucose. In diabetics, higher α-amylase activity can accelerate the breakdown of carbohydrates, resulting in a rise in blood glucose levels.[18–20]

Similarly, PTP1B (Human Tyrosine Phosphatase-1B) is considered an important target against type II diabetes mellitus.[21–24] In the human body, PTP1B reduces leptin and insulin signaling and has demonstrated involvement in inflammation responses. PTPIB dephosphorylates IRS-1 (Insulin Receptor Substrate-1) and IR (Insulin Receptor), causing insulin resistance.[25–27] Therefore, suppression of this protein can improve insulin resistance in the body.[28] Enzymatic and *in silico* studies predict that synthesized inhibitors can interact with the active site to suppress the catalytic efficiency of α-amylase and PTPIB. The inhibition of α-amylase restricts the conversion of starch to glucose, resulting in a reduction of glucose absorption in the blood. Likewise, the inhibition of PTP1B results in the sustained insulin receptor phosphorylation and improved Akt/IRS-1/PI3K signaling (Fig. 1).[29–33]

There are several drugs, such as acarbose **1** (containing valienamine fragment (with 1*S*,2*S*,3*R*,6*S* configuration) alongside three sugars with configurations 2*R*,3*S*,4*S*,5*R*,6*R*,2*R*,3*S*,4*R*,5*R*,6*R*, and 2*R*,3*S*,4*R*,6*R*[34–36]), voglibose **2** [37–39] (1*S*,2*S*,3*S*,4*S*,5*S* configuration) and miglitol **3** (2*R*,3*R*,4*R*,5*S* configuration),[40,41] that have been widely used for the inhibition of α-amylase,

[a]*Department of Chemistry, Government College University Faisalabad, Faisalabad 38000, Pakistan. E-mail: fawad.zahoor@gcuf.edu.pk*
[b]*Department of Biochemistry, Government College University Faisalabad, Faisalabad 38000, Pakistan*

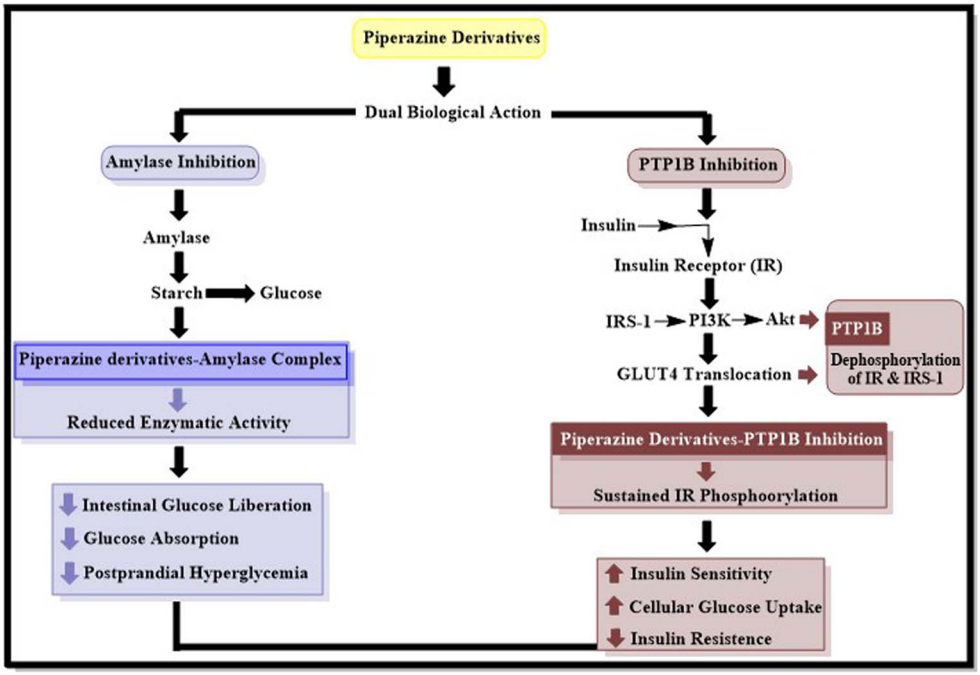

Fig. 1 Anti-diabetic dual action of synthesized compounds *via* enzyme inhibition and insulin signal amplification.

which are accountable for interrupting the hydrolysis of larger units (disaccharides and oligosaccharides) into smaller monosaccharide units. Despite their clinical usage, there are multiple adverse consequences, such as gastrointestinal distress, diarrhea, flatulence, and meteorism, resulting in discontinuation of treatment.[42] Hence, to ensure effectiveness, they are frequently utilized together with other antidiabetic agents. Therefore, it is essential to identify new strategies for the management of diabetes with no or low potential for adverse effects.[43–45]

Heterocycles containing nitrogen are an important class of organic compounds due to their high pharmacological and biological importance.[46–48] Notably, piperazine, an important six-membered heterocycle having two nitrogen atoms at the 1 and 4 positions, has a major impact in pharmaceutical research.[49–51] This moiety is found in a plenty of renowned medications with broad pharmacological effects, such as antidepressants, cardio-protectors, antianginals and antihistamines. Different piperazine derivatives **4** & **5** also displayed antidiabetic potential. A piperazine moiety containing drug teneligliptin **6** has been approved as an oral DPP-4 inhibitor in some countries, for the treatment of type-II diabetes (Fig. 2).[52–54]

Additionally, 1,2,4-triazoles are globally acknowledged as important pharmacophores and have been widely investigated in antidiabetic drug design. Recent literature revealed that several triazole derivatives *i.e.*, derivative **7** ($IC_{50} = 0.53 \pm 0.14$ nM) and derivative **8** ($IC_{50} = 0.97 \pm 0.47$ μM) exhibited antidiabetic potential against α-amylase.[55,56] Moreover, 1,2,4-triazoles have also been explored against multiple anti-diabetic targets such as PTP1B (**9**, $IC_{50} = 6.45$ μM) and DPP-4 (**10**, $IC_{50} = 1.50$ nM), highlighting their wider scope in the treatment of diabetes.[57,58]

The fragment-based drug design (FBDD) is considered an important strategy for the synthesis of biologically important hybrids. In this study, the FBDD approach was used to merge distinct pharmacophores such as piperazine, triazole and benzofuran into a single molecule to attain improved therapeutic effect.[59,60] The newly designed hybrids were biologically evaluated against α-amylase. Network pharmacology analysis was conducted, spotting PTP1B (Protein Tyrosine Phosphatase 1B) as an important target linked with insulin resistance. Additionally, molecular docking, MD simulation, MMPBSA, PCA, DCCM and FEL analyses were carried out to analyze the interaction and stability of the synthesized complexes. ADMET and DFT studies were also carried out to assess drug-likeness and electronic properties, respectively. These outcomes establish a firm basis for future improvements and the formation of more efficacious anti-diabetic molecules.

2 Results and discussion

2.1 Chemistry

The piperazine–tethered triazole hybrids **10a–10j** were synthesized as per reported methodology, depicted in Scheme 1.[61] According to it, *tert*-butyl 4-(2-bromoacetyl)piperazine-1-carboxylate **12** was allowed to react with substituted benzofuran triazoles **11a–11j** using K_2CO_3, KI and DCM at room temperature. The desired products **13a–13j** were obtained in good to excellent yields (61–78%) (Fig. 3).

2.2 Network pharmacology analysis

2.2.1 PPI network construction and hub gene identification. The PPI network was developed to analyze functional

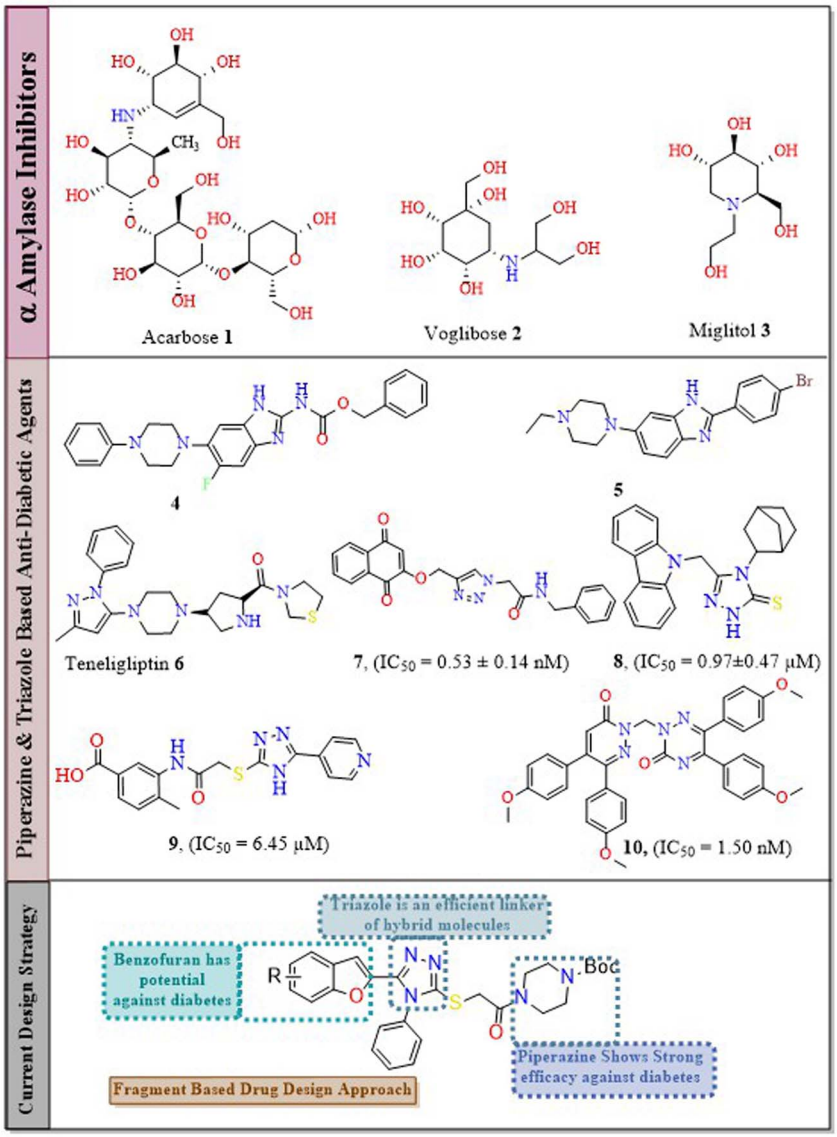

Fig. 2 Previously reported anti-diabetic agents and current design strategy.

interactions using Cytoscape and String.[62] A highly interconnected network was formed, indicating high cross-talk among protein targets. The hub gene analysis revealed that PTPN1 emerged as the most distinguished gene among multiple key genes interuupting such as NFKB1, NFE2L2, PTGS2, and HIF1A. The core position of PTPN1 in the PPI network signals its central role in various biological pathways connected to diabetes (Fig. 4).[63]

PTPN1 represents protein tyrosine phosphatase non-receptor type 1 (PTP1B), a well-recognized inhibitor of insulin

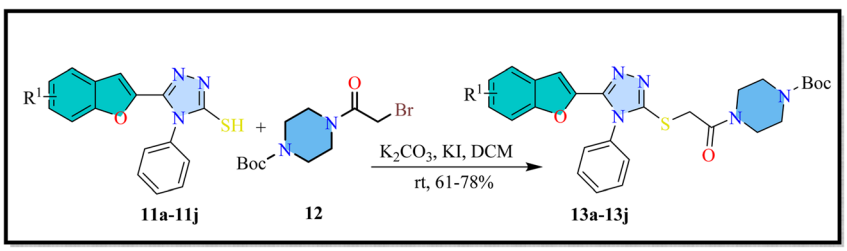

Scheme 1 Synthetic protocol for the preparation of triazole–tethered piperazine conjugates 13a–13j.

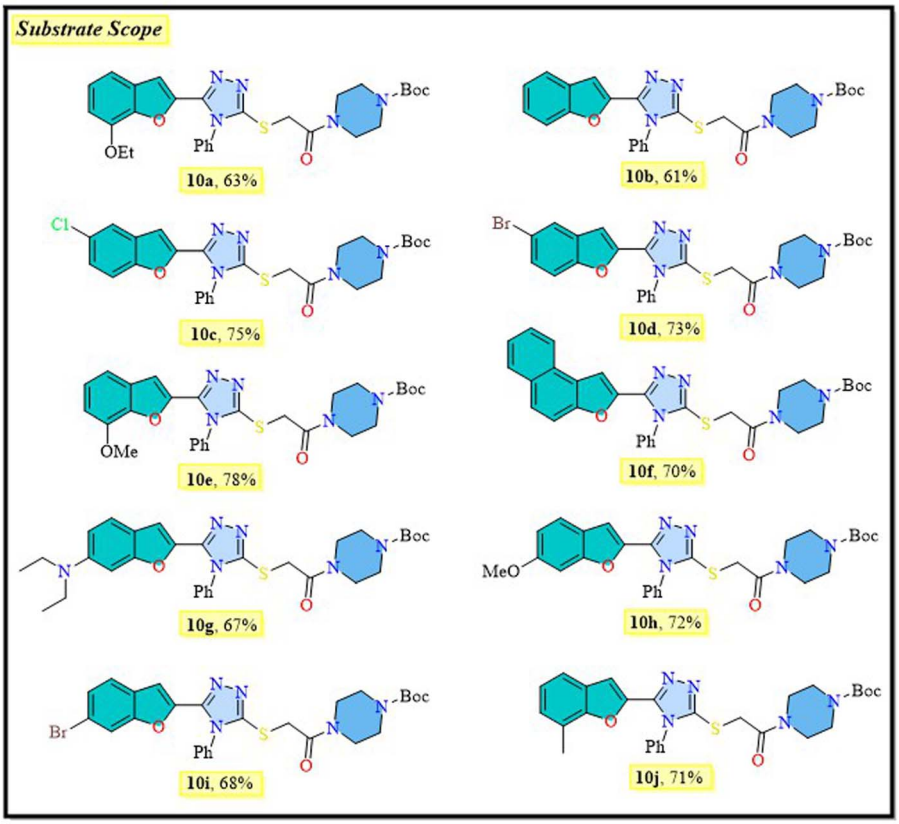

Fig. 3 Substrate scope of piperazine–triazole conjugates **13a–13j**.

receptor (IR) and IR substrate signaling.[64] Excessive activation of PTPN1 results in disrupted insulin signaling that leads to insulin resistance.[65] Therefore, the suppression of PTPN1 (PTP1B) has been broadly acknowledged as encouraging a therapeutic approach to improve glucose homeostasis and insulin sensitivity. HIFIA plays a key role in glucose regulation, which is deregulated in hyperglycemic tissues.[66] The PPI interactions of PTPN1 indicated a strong connection with NFE2L2,

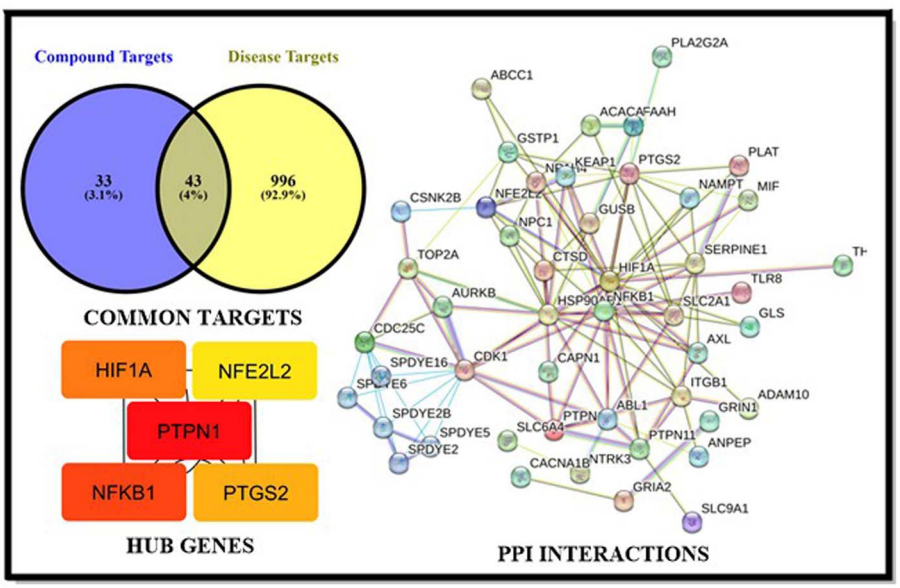

Fig. 4 Identification of common targets, Hub gene and PPI interaction analysis.

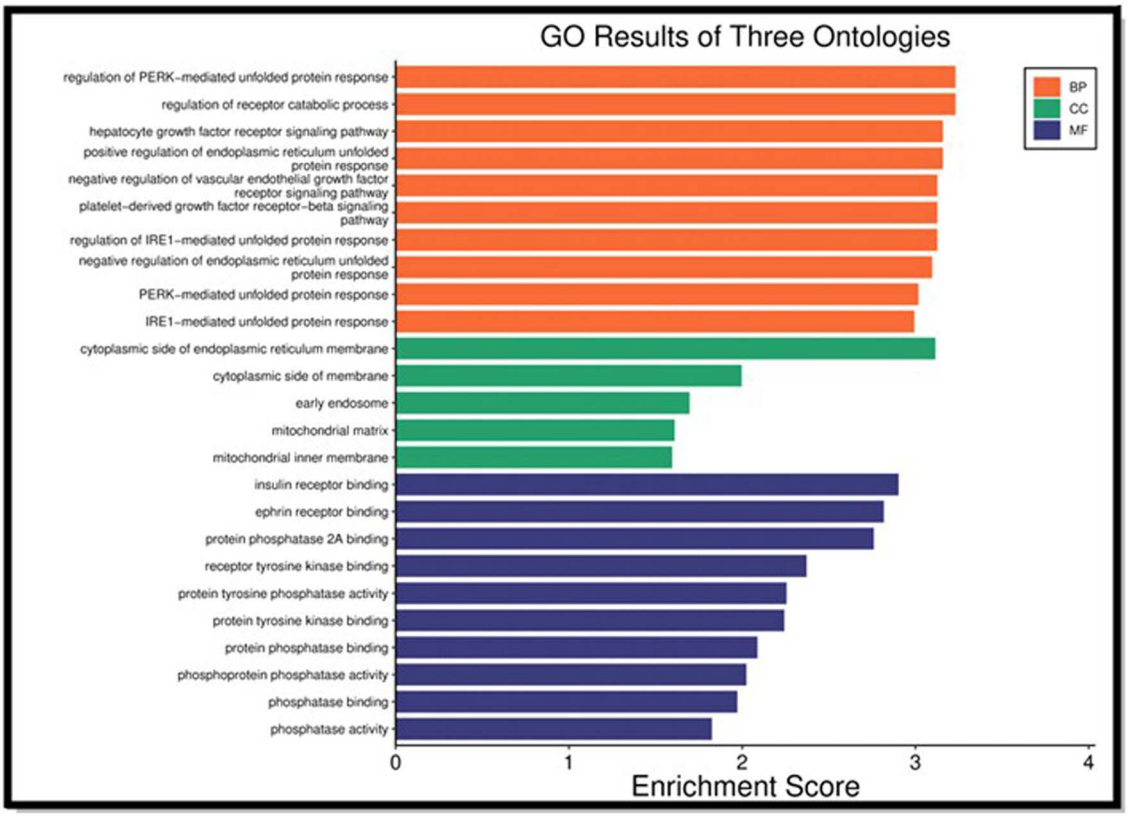

Fig. 5 GO Enrichment Analysis of target genes.

which is considered to be a key regulator of oxidative stress and antioxidant defense.[67] Different research revealed that oxidative stress plays a significant role towards the progression of β-cell impairment along with insulin resistance.[68] These interactions regulate redox homeostasis and improve insulin signaling. Furthermore, PTPN1 also contributed toward PTGS2 and NFKB1 signaling, which emphasizes the engagement of PTPN1 in inflammation-induced insulin resistance.[69]

2.2.2 KEGG pathway and GO enrichment analysis. The GO enrichment analysis uncovered that the target genes exhibited significant enrichment. In the biological process, enrichment analysis revealed that enrichment terms are predominantly allocated with process concerned with unfolded protein response (UPR) and endoplasmic reticulum.[70] Both of them are key players in insulin resistance. The long-term ER stress impairs insulin signaling and boosts inflammation. These enrichments suggest that PTPN1 might affect ER stress signaling, thus enhancing insulin sensitivity.[71] The enriched terms in cellular components are mainly associated with the mitochondrial matrix, cytoplasmic side membrane, early endosome, and cytoplasmic side of the ER membrane.[72] These associations are linked with functional property and intracellular localization of PTPN1, tied to the cytoplasmic ER membrane by making direct interactions with the insulin receptor. The analysis of molecular function revealed that there is a strong enrichment of terms associated with insulin receptor binding, phosphatase binding, protein tyrosine phosphatase activity, and kinase binding. These results explicitly endorse the function of PTPN1 as an insulin receptor regulator *via* the dephosphorylation of tyrosine residues (Fig. 5).[73]

The KEGG pathway analysis validated the contribution of diabetes related signaling routes.[74] The most substantially enriched route involved the insulin signaling and resistance pathway alongwith other oxidative stress pathways (Fig. 6 and S21, SI).[75] Particularly, PTPN1 is explicitly associated with insulin regulation and resistance, during which it suppresses the insulin receptor substrate phosphorylation and insulin receptor.[76] The suppression of PTPN1 is thus anticipated to improve glucose uptake, GLUT4 translocation and PI3K-Akt signaling.[77] Moreover, oxidative stress also contributed to insulin resistance due to ROS (reactive oxygen species).[68] It was concluded from the KEGG and GO enrichment analysis that PTPN1 suppression might be beneficial in reducing oxidative stress, along with insulin signaling improvement.

2.3 Molecular docking analysis

All the synthesized compounds were docked against two primary targets (α-amylase and PTP1B) to evaluate their inhibitory potential. The docking protocols were validated through the determination of RMSD (Root Mean Square Deviation). For this purpose, the native ligand was redocked and upon superimposition, an RMSD value of 0.66 Å (<2.0 Å) was calculated. The low RMSD value generally verifies docking validity and conformational stability (Fig. 7).[78,79] The compounds **13a–13j**

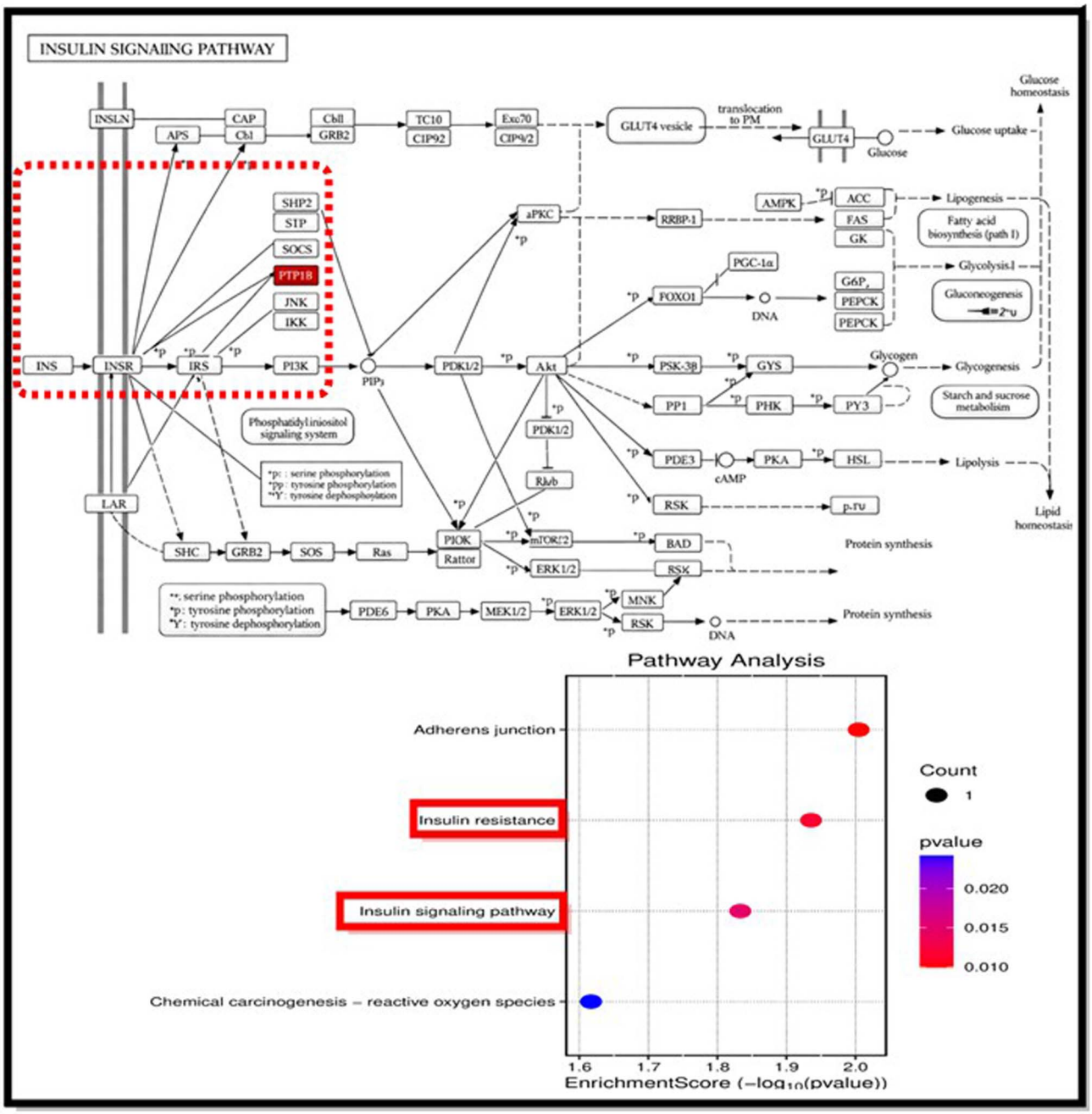

Fig. 6 Representation of insulin signaling pathway *via* KEGG analysis.

gave docking scores in a range from −8.8 to −10.5 kcal mol^{-1} against α-amylase (2QV4). Similarly, compounds **13a–13j** exhibited binding affinities in a range from −7.2 to −8.0 kcal mol^{-1} against PTP1B (1NNY). Among all, compounds **13c** and **13e** gave higher docking scores, even better than standard acarbose (Table 1).

The conformational analysis revealed that both compounds, **13c** and **13e** interacted with α-amylase by making different key interactions with active site residues such as GLU233, ASP197 (Fig. 8).[80] The compound **13c** made significant electrostatic and aromatic contacts with the catalytic site of α-amylase. The

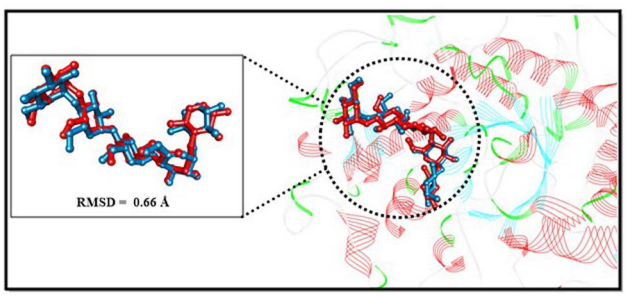

Fig. 7 Validation of docking protocols by superimposition of redocked ligand (blue) with native ligand (red).

Table 1 Binding affinities of screened compounds **13a–13j**

Compounds	α-Amylase (2QV4) kcal mol^{-1}	PTP1B (1NNY) kcal mol^{-1}
13a	−9.2	−7.6
13b	−8.7	−7.3
13c	−10.5	−8.0
13d	−8.8	−7.4
13e	−9.7	−7.8
13f	−8.5	−7.5
13g	−8.8	−7.3
13h	−9.4	−7.5
13i	−9.2	−7.2
13j	−9.5	−7.3
Acarbose	−8.1	−7.4

strong interaction of **13c** with the residue GLU233 is substantial due to its involvement in the acid-base chemistry of glycosidic bond breakage as reported by Neves *et al.*[81] Likewise, the π-cationic contacts of ligand **13c** with HIS201 can change the protonation state for further catalytic disruption.[82] The interactions of the piperazine cage with TYR62 and TRP59 potentially inhibit the starch substrate binding,[83] which makes **13c** a competitive inhibitor of α-amylase (Table 2). Similarly, LEU235 and LEU162 interacted with ligand **13c**, thus destabilizing the catalytic environment.[84] Additionally, compound **13e** broadly occupied the active site. It established hydrogen bonding interactions with LYS200 and GLN63 near the entrance of the catalytic site.[85,86] The compound **13e** disrupts the electrostatic environment by interacting with ASP198 and GLU233 residues.[87] The residues TYR151 and TRP59 established hydrogen bonding and π-sigma interactions with the aromatic site and Boc functionality of compound **13e** (Fig. 9) as explained by Gautam *et al.*[88] In comparison, the reference compound acarbose made strong conventional hydrogen bonding and carbon-hydrogen bonding interactions with GLN63, HIS101, ASN105, ALA106, HIS299, THR163, ASP300, TYR62, GLU23, ALA198 and GLU233 at distances of 2.59 Å, 2.59 Å, 2.73 Å, 2.08 Å, 2.21 Å, 2.18 Å, 2.59 Å, 2.78 Å, 2.77 Å, 3.74 Å and 3.31 Å respectively (Fig. 12).

The conformational analysis of compounds **13c** and **13e** demonstrated that they adopt a stable binding conformation within the active site of PTP1B (1NNY) (Fig. 10).[89] PTPIB facilitates phosphorylation of phosphotyrosine residues on insulin

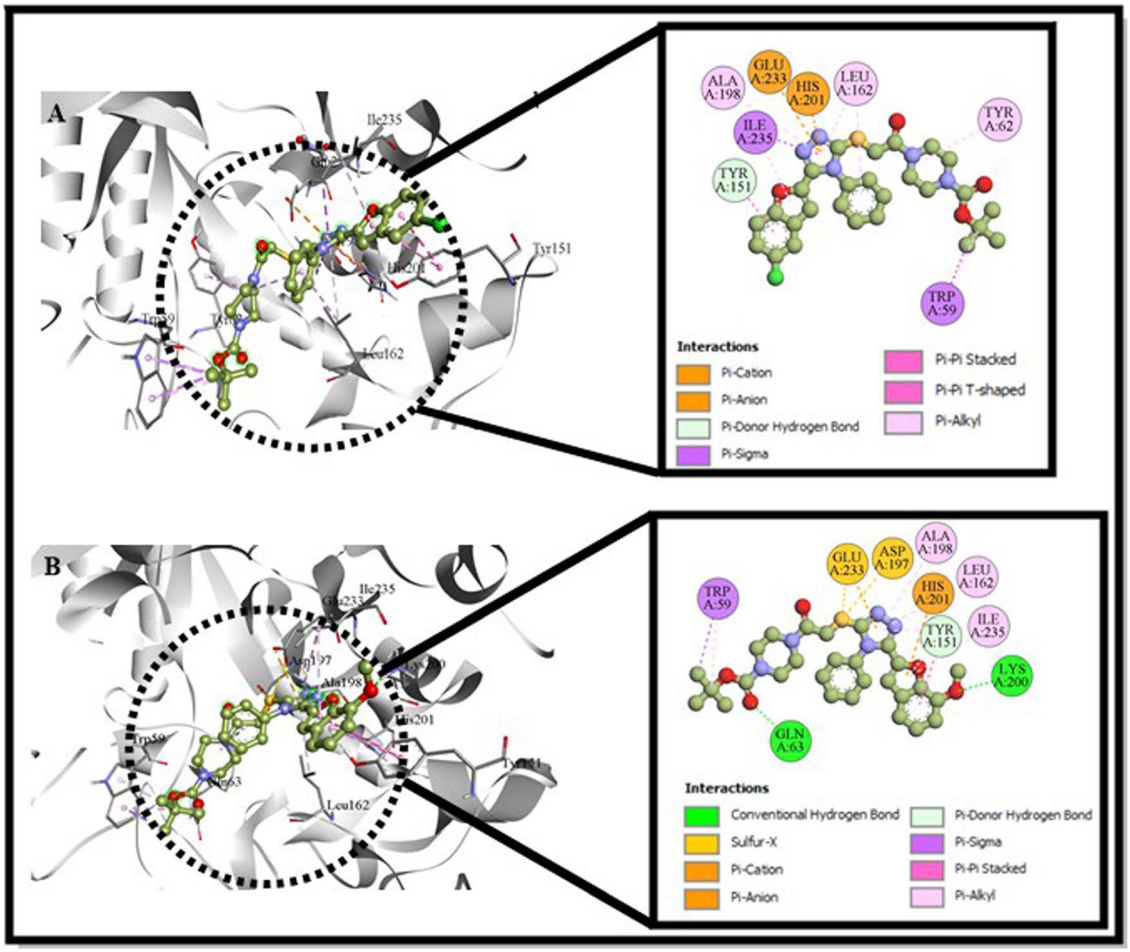

Fig. 8 Binding analysis of compounds **13c** (A) & **13e** (B) with α-amylase (2QV4).

Table 2 Interactions of different residues of α-amylase with **13c** & **13e**

Compounds	Residue	Distance (Å)	Interactions	Type
13c	HIS201	3.59	Electrostatic	π-Cation
	GLU233	4.41	Electrostatic	Pi-anion
	TYR151	2.84	H-Bond	π-Donor hydrogen bond
	ILE235	3.86	Hydrophobic	π-Sigma
	TRP59	3.75	Hydrophobic	π-Sigma
	TRP59	3.67	Hydrophobic	Pi-sigma
	TYR151	4.04	Hydrophobic	π–π Stacked
	TYR151	4.68	Hydrophobic	π–π Stacked
	HIS201	4.6	Hydrophobic	π–π T-shaped
	TRP59	4.72	Hydrophobic	π-Alkyl
	TRP59	4.38	Hydrophobic	π-Alkyl
	TYR62	5.42	Hydrophobic	π-Alkyl
	ILE235	4.7	Hydrophobic	π-Alkyl
13e	GLN63	2.28	H-Bond	Conventional H-bond
	LYS200	2.53	H-Bond	Conventional H-bond
	ASP197	3.27	Other	Sulfur-X
	GLU233	3.00	Other	Sulfur-X
	HIS201	4.37	Electrostatic	π-Cation
	GLU233	4.14	Electrostatic	π-Anion
	TYR151	2.52	H-Bond	π-Donor hydrogen bond
	TRP59	3.66	Hydrophobic	π-Sigma
	TYR151	4.21	Hydrophobic	π-π Stacked
	TYR151	5.08	Hydrophobic	π-π Stacked
	TRP59	4.32	Hydrophobic	π-Alkyl
	TRP59	4.07	Hydrophobic	π-Alkyl
	ILE235	5.17	Hydrophobic	π-Alkyl
Acarbose	GLN63	2.59	H-Bond	Conventional H-bond
	HIS101	2.59	H-Bond	Conventional H-bond
	ASN105	2.73	H-Bond	Conventional H-bond
	ALA106	2.08	H-Bond	Conventional H-bond
	HIS299	2.21	H-Bond	Conventional H-bond
	THR163	2.18	H-Bond	Conventional H-bond
	ASP300	2.59	H-Bond	Conventional H-bond
	TYR62	2.78	H-Bond	Conventional H-bond
	GLU23	2.77	H-Bond	Conventional H-bond
	ALA198	3.74	H-Bond	Carbon H-bond
	GLU233	3.31	H-Bond	Carbon H-bond

receptor *via* positive charge residues within the active site.[73] The residues LYS120 and LYS116 interacted with the aromatic region of **13c** *via* conventional hydrogen bonding interactions (Fig. 11).[90] The interactions of these residues stabilize the positive residues, thus reducing the catalytic activity and improving insulin signaling.[90] Similarly, the other residues GLY220, GLY183, ALA217, and TYR46 interacted with compound **13c**, promoting interference with substrate conformation, restricting conformational flexibility, and helping in inhibitor retention within the binding pocket. Similarly, compound **13e** made π-cationic contact with LYS116 and hydrogen bonding interactions with LYS120 *via* the aromatic region. Similarly, other critical residues such as GLY183, TYR46, and ALA217 interacted *via* hydrophobic and hydrogen bonding interactions at distances of 2.25 Å, 5.1 Å, and 4.45 Å (Table 3).[91] In comparison, the standard acarbose formed conventional hydrogen bonding interactions with ARG24, TRP179, GLY183, ARG221, ARG221 and GLY183 (Fig. 12).

2.4 Molecular dynamics simulation analysis

The potent compounds were selected to assess the overall stability of complexes during the 500 ns simulation time. The results were interpreted through measurement of RMSD, RMSF, contact analysis, and rGyr.

2.4.1 RMSD analysis of 13c and 13e. The structural stability of complex **13c_2QV4** and **13e_2QV4** was evaluated *via* RMSD. In the case of complex **13c_2QV4**, the RMSD initially increased during the preliminary equilibration step. After the initial deviation period, the complex stabilized itself between 2.1 and 2.6 Å. Likewise, the ligand of complex **13c_2QV4** followed the same deviation pattern and stably bound within the active site. Similarly, the protein of complex **13e_2QV4** exhibited stable RMSD within a range of 2.0–2.3 Å. The ligand part of complex **13e_2QV4** displayed marked deviation due to conformational changes. Overall, both ligands maintained stable conformations within the active site of α-amylase (Fig. 13). Additionally, the RMSD of Cα atoms of PTP1B was determined to assess the

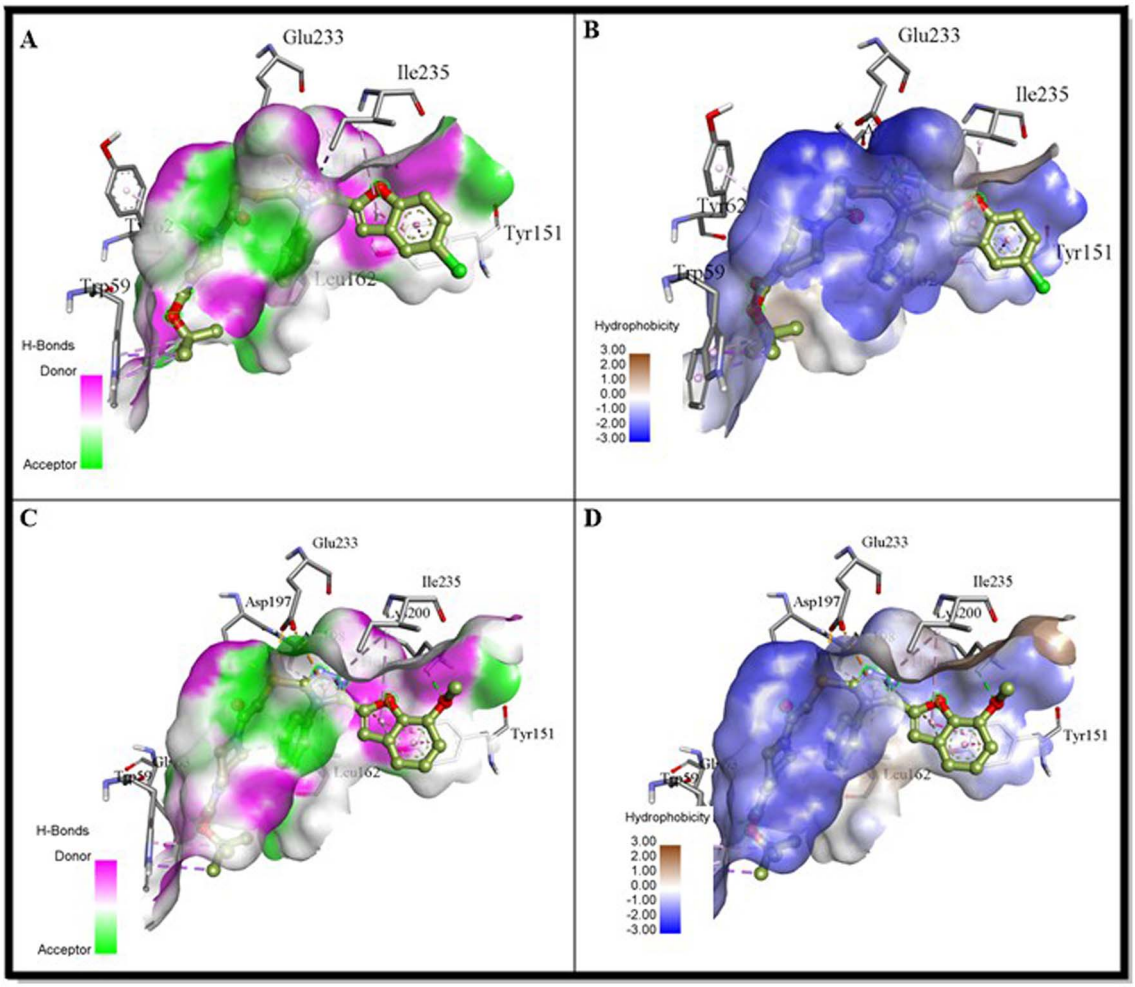

Fig. 9 (A & B) H-bonding and hydrophobic interactions of **13c** with α-amylase (2QV4). (C &D) (B) H-bonding and hydrophobic interactions of **13e** with α-amylase (2QV4).

stability of the backbone. The Cα atoms of PTP1B made stable conformations with an RMSD range from 2.5 to 3.0 Å. The ligand **13c** firmly attached within the binding site with some minor deviations. Similarly, complex **13e_PTP1B** displayed stable interaction around 2.7–3.1 Å after initial deviation. In both complexes, stable binding interactions were formed within the active site of PTP1B (Fig. 14).

2.4.2 RMSF analysis of 13c and 13e. The individual residual flexibility was determined through RMSF. It was observed from the complex **13c_2QV4** that most of the residues exhibited low RMSD (<1.5 Å) due to restricted fluctuations. Higher fluctuations were observed around the loop region that has inherent flexibility. Similarly, the same fluctuation profile was observed for **13e_2QV4** (Fig. 13). Both complexes displayed minimal fluctuations with the binding site residues of α-amylase. The RMSF analysis of **13c_PTP1B** revealed that the majority of residues exhibited constrained backbone fluctuations (<1.5 Å). The loop and terminal residues exhibited higher fluctuations. Similarly, **13e_PTP1B** demonstrated slightly higher fluctuations around the loop region than complex **13c_PTP1B** (Fig. 14).

2.4.3 Interpretation of contacts between ligand and protein. The ligand–protein contacts analysis was performed to probe the type of interactions formed by the ligands with the active site of target proteins. Persistent key interactions were observed when complex **13c** made strong interactions with active site residues GLN63, TRP59, TYR151, TRP58 and HIS201 of α-amylase. The binding profile was dominated by hydrophobic as well as hydrogen bonding interactions. It was observed from time-resolved interaction analysis that uniform interactions were formed throughout simulation time (Fig. 15). Similarly, the dynamic behavior of complex **13e**, as it displayed irregular interactions, was compared with that of **13c** (Fig. 16). The 2D interaction supported the evidence that both complexes maintained stable interactions within the catalytic site of α-amylase (Fig. 17). The complex **13c** interacted with ARG254, ILE163 and ASP181. Hydrophobic and hydrogen bonding contacts surround these interactions, thereby playing significant role towards complex's stability. The timeline of interactions revealed that **13c** made overall stable contacts despite several fluctuations of residues within the active site of PTP1B (Fig. 18). Similarly, **13e** made strong interactions with residues

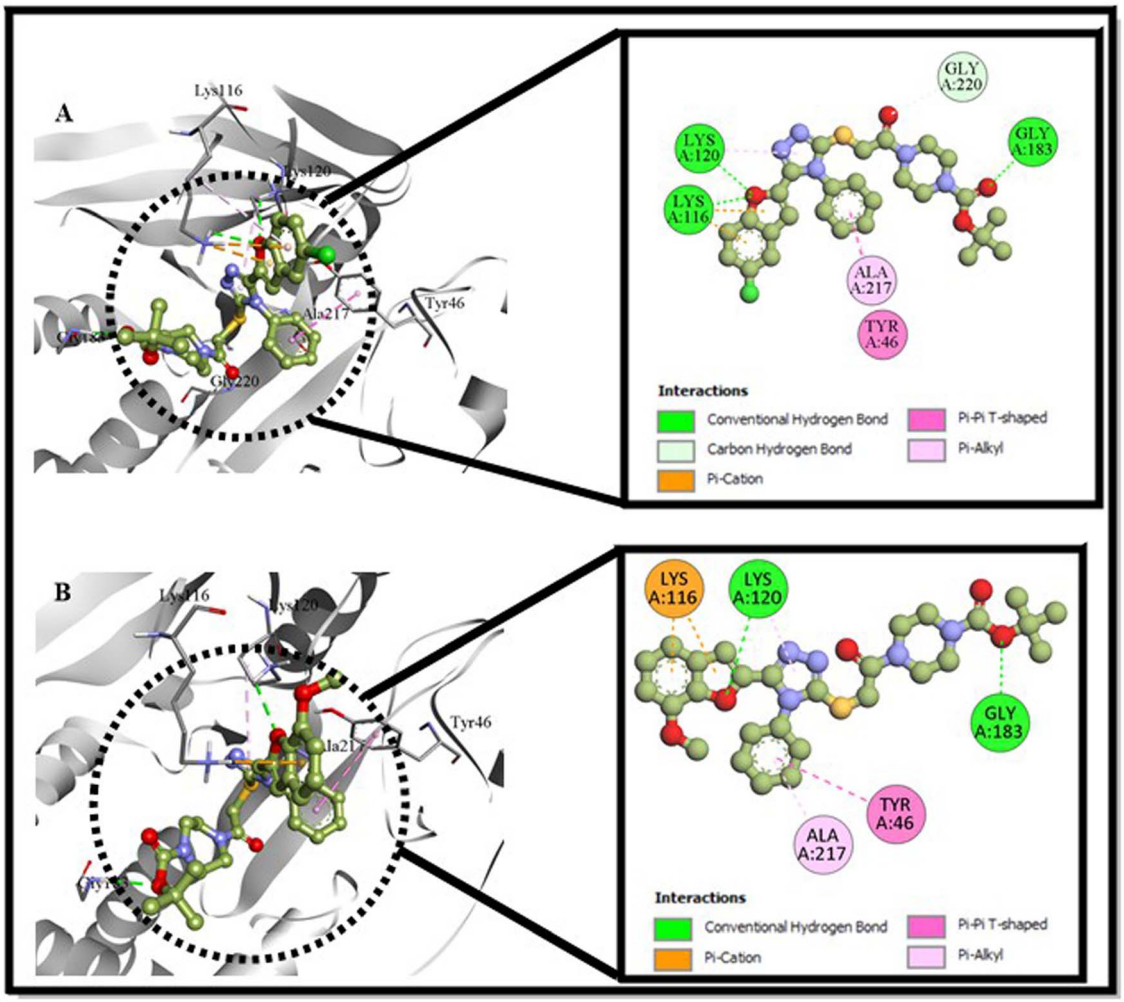

Fig. 10 Binding analysis of compounds **13c** (A) & **13e** (B) with PTP1B (1NNY).

ILE219, PRO31, VAL49, ASP48 and TYR46 *via* both hydrogen and hydrophobic interactions (Fig. 19). The 2D plot revealed that both compounds are involved in multiple interactions within the catalytic site (Fig. 20).

2.4.4 Radius of gyration. The overall compactness of complexes **13c** and **13e** was determined through radius of gyration (rGyr). Stable rGyr was observed throughout the simulation time for compound **13c** in complex with α-amylase (Fig. 21). The complex **13e** exhibited marginally higher fluctuations. However, in both situations, the protein established well-folded and compact conformations within the binding pocket of α-amylase. Additionally, the **13c_PTP1B** displayed observable fluctuations in rGyr due to conformational adjustments in the protein. In complex **13e_PTP1B**, a bit higher fluctuations as compared to **13c_PTP1B** complex were noticed due to higher flexibility. It was observed that the compound **13c** binds with both α-amylase and PTP1B receptor, which exhibited higher compactness and stability (Fig. 21).

2.5 Estimation of binding free energies through MMPBSA

The binding free energies of the complexes were determined by using MMPBSA analysis. The complex **13c_2QV4** exhibited a higher binding energy of −43.71 kcal mol^{-1}. Similarly, complex **13e_2QV4** illustrated −26.41 kcal mol^{-1} binding energy. Additionally, the complex **13c_PTP1B** and **13e_PTP1B** demonstrated binding energies of −20.69 kcal mol^{-1} and −16.08 kcal mol^{-1}, correspondingly (Table 4). The individual component analysis revealed that van der Waals interactions are the major contributor among all individual binding components. This indicates the contribution of hydrophobic interactions in the stabilization of all complexes. WCA energy and electrostatic energies contributed generously to the stabilization of the complex; however, polar solvation energy contributed unfavorably to the stability of the complex. Overall, the complex **13c** exhibited higher stability within the binding pocket of target proteins, thus indicating more substantial inhibitory potential (Fig. 22).

2.6 DCCM analysis

The correlated and anti-correlated movements with active site residues upon binding with ligands were assessed through DCCM (Dynamic Cross-Correlation Matrix). Both complexes *i.e.*, **13c_2QV4** and **13e_2QV4** exhibited positive correlation across the diagonal, indicating the structural stability and

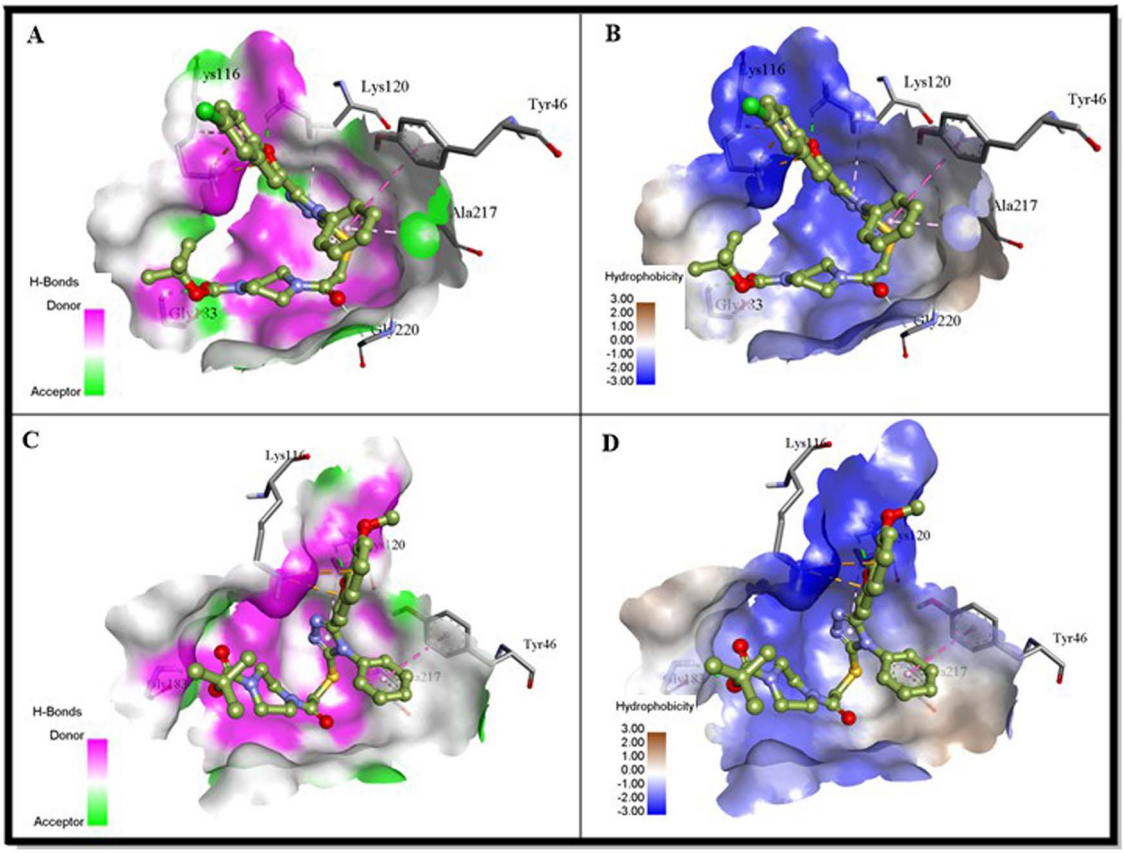

Fig. 11 (A & B) Hydrogen bonding and hydrophobic interactions of **13c** with PTP1B (1NNY). (C &D) Hydrogen bonding and hydrophobic interactions of **13e** with PTP1B (1NNY).

Table 3 Interactions of different residues of PTP1B (1NNY) with **13c** & **13e**

Compounds	Residue	Distance (Å)	Interactions	Type
13c	LYS116	2.71	H-Bond	Conventional H-bond
	LYS120	2.5	H-Bond	Conventional H-bond
	GLY183	2.28	H-Bond	Conventional H-bond
	GLY220	3.4	H-Bond	Carbon H-bond
	LYS116	3.48	Electrostatic	π-Cation
	LYS116	3.03	H-Bond; electrostatic	π-Cation; π-donor H-bond
	TYR46	5.13	Hydrophobic	π–π T-shaped
	LYS116	5.36	Hydrophobic	π-Alkyl
	LYS120	4.97	Hydrophobic	π-Alkyl
	ALA217	4.49	Hydrophobic	π-Alkyl
13e	LYS120	2.72	H-Bond	Conventional H-bond
	GLY183	2.25	H-Bond	Conventional H-bond
	LYS116	3.44	Electrostatic	π-Cation
	LYS116	3.02	H-Bond; electrostatic	π-Cation, π -donor H-bond
	TYR46	5.1	Hydrophobic	π–π T-shaped
	LYS120	5.11	Hydrophobic	π-Alkyl
	ALA217	4.45	Hydrophobic	π-Alkyl
Acarbose	ARG24	2.34	H-Bond	Conventional H-bond
	TRP179	2.48	H-Bond	Conventional H-bond
	GLY183	2.81	H-Bond	Conventional H-bond
	ARG221	2.25	H-Bond	Conventional H-bond
	ARG221	2.36	H-Bond	Conventional H-bond
	GLY183	2.59	H-Bond	Conventional H-bond

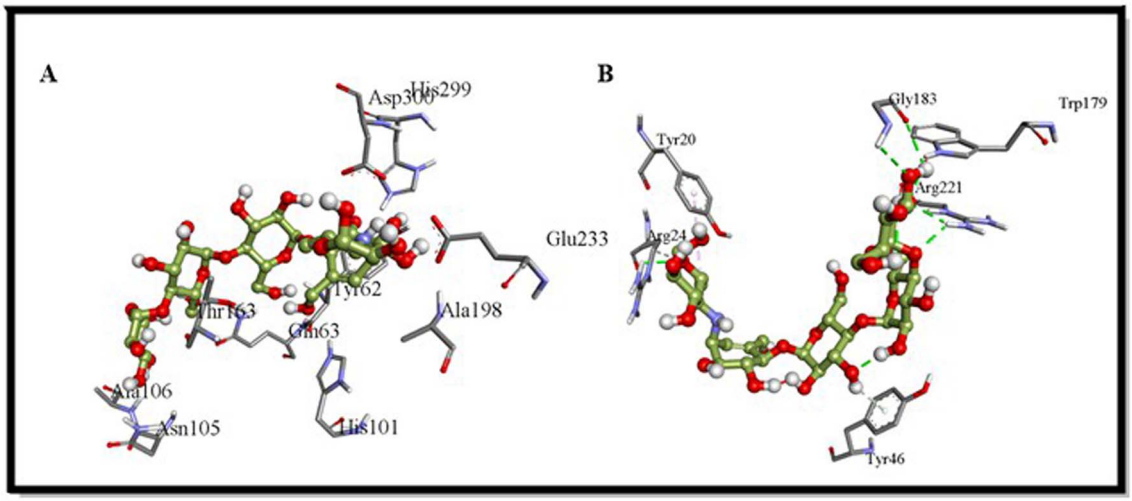

Fig. 12 Interactions of compound acarbose with 2QV4 (A) and 1NNY (B).

synchronized motion surrounding residues. Similarly, the complexes **13c_PTP1B** and **13e_PTP1B** showed a noticeable correlation, as complex **13c_PTP1B** exhibited marked correlated movements, suggesting enhanced internal stability. In contrast, higher anti-correlated regions were observed in the **13e** complex due to conformational fluctuations. Generally, the complex **13c** demonstrated favorably correlated movements with both receptors (Fig. 23).

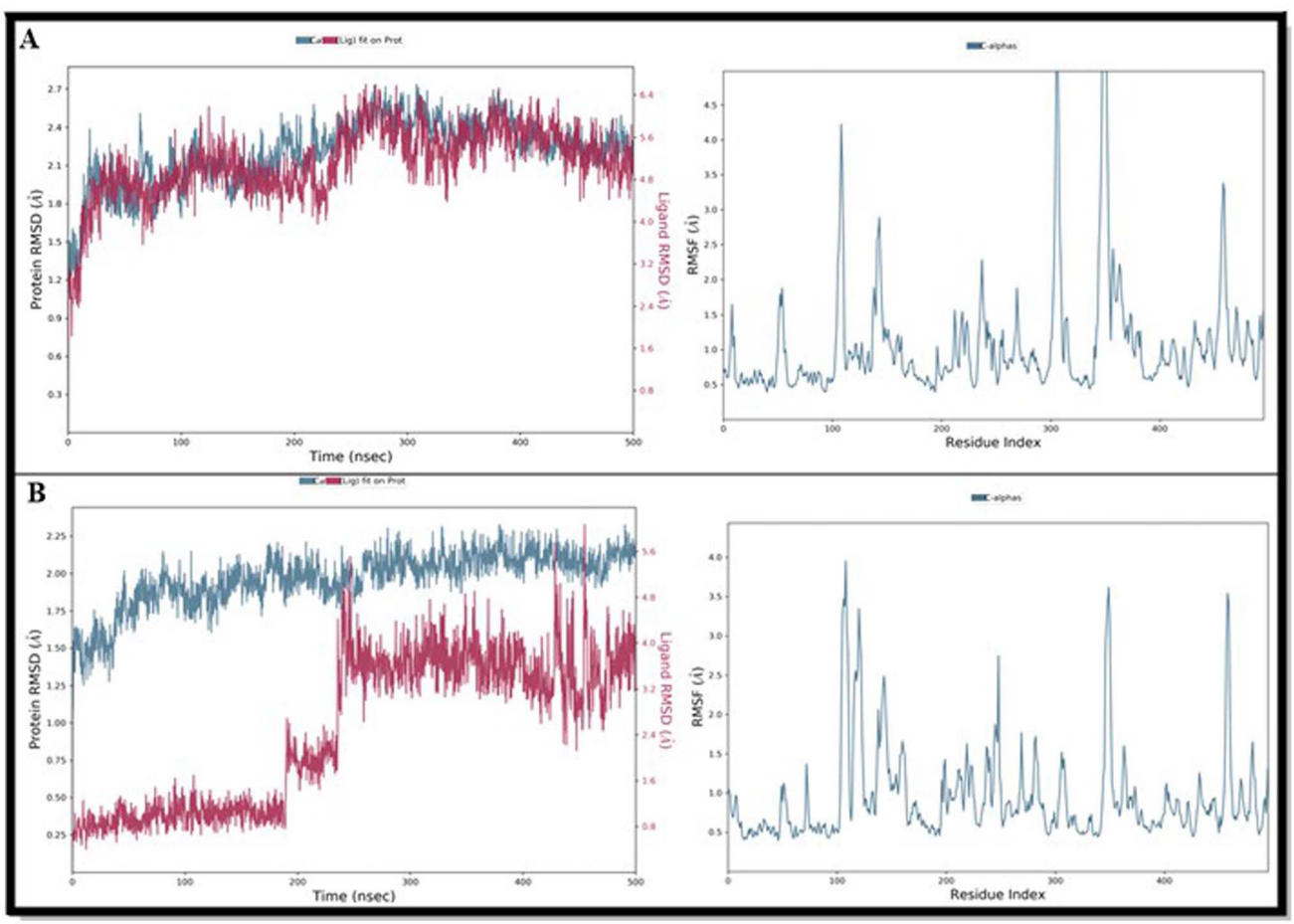

Fig. 13 RMSD and RMSF calculations of complex **13c_2QV4** (A) and **13e_2QV4** (B).

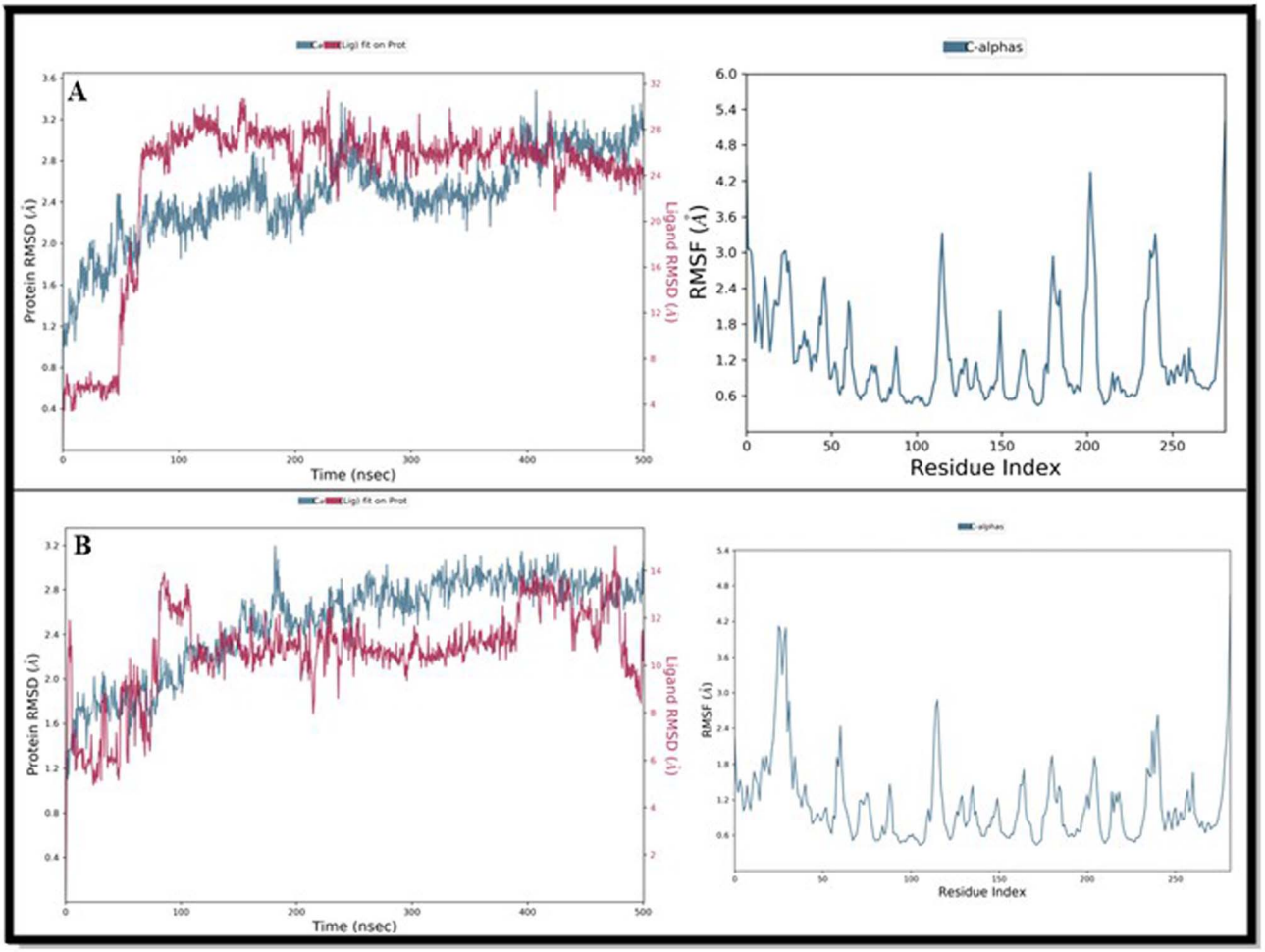

Fig. 14 RMSD and RMSF calculations of complex **13c_PTP1B** (A) and **13e_PTP1B** (B).

2.7 PCA and FEL analysis

The key collective movements observed throughout the simulation time were investigated through PCA (Principal Component Analysis). Among both **13c_2QV4** and **13e_2QV4** complexes, the complex **13c_2QV4** occupied a more distinct and compact motion along PC1 and PC2. Likewise, **13e_2QV4** showed higher conformational variability, suggesting more flexibility. Additionally, **13c_PTP1B** exhibited constrained structural dynamics due to more compact clustering across PC1 and PC2. Similarly, **13e_PTP1B** demonstrated scattered distribution along PC2 and PC1 (Fig. 24). Furthermore, the thermodynamic stability of individual conformation was evaluated through FEL (Free Energy Landscape). Among all, complex **13c_2QV4** and **13c_PTP1B** exhibited distinct and intense global minima, suggesting thermodynamically stable conformations. The deeper basins indicated the stable binding with low-energy conformations. Likewise, complexes **13e_2QV4** and **13e_PTP1B** showed a higher energy barrier between different states. Overall, it was observed from PCA, DCCM, and FEL analysis that complex **13c** illustrated enhanced correlated dynamics, higher dynamic stability, and favorable energy minima (Fig. 25).

2.8 Density functional Theory analysis

The stability of synthesized compounds **13c** and **13e** was assessed through DFT studies. A Gaussian program was used to perform all the calculations. The optimization of structures was done by using the B3LYP functional with the 631G(d) basis set.

2.8.1 Geometry optimization of compounds 13c and 13e. The geometry-optimized structures of compounds **13c** and **13e** were depicted in Fig. 26. The geometry optimization gave stable structures, which were used to calculate the bond angles and bond lengths as mentioned in the Table 5. It was observed from the geometry optimization that both compounds **13c** and **13e** adopted a non-planar conformation because of the aromatic ring and heteroatoms, leading to electronic and steric effects. All of the observed bond lengths were noted to be in the expected range for heterocyclic compounds.

2.8.2 Frontier molecular orbital analysis. The chemical reactivity and electronic properties of the synthesized compounds **13c** and **13e** were determined through FMO. The HOMO energy for compound **13c** was noted to be −0.218 eV and the LUMO is found at −0.05 eV. Likewise, the HOMO energy gap in compound **13e** is found at −0.205 eV, while LUMO is located at −0.047 eV. The energy gaps for compounds **13c** and **13e** were

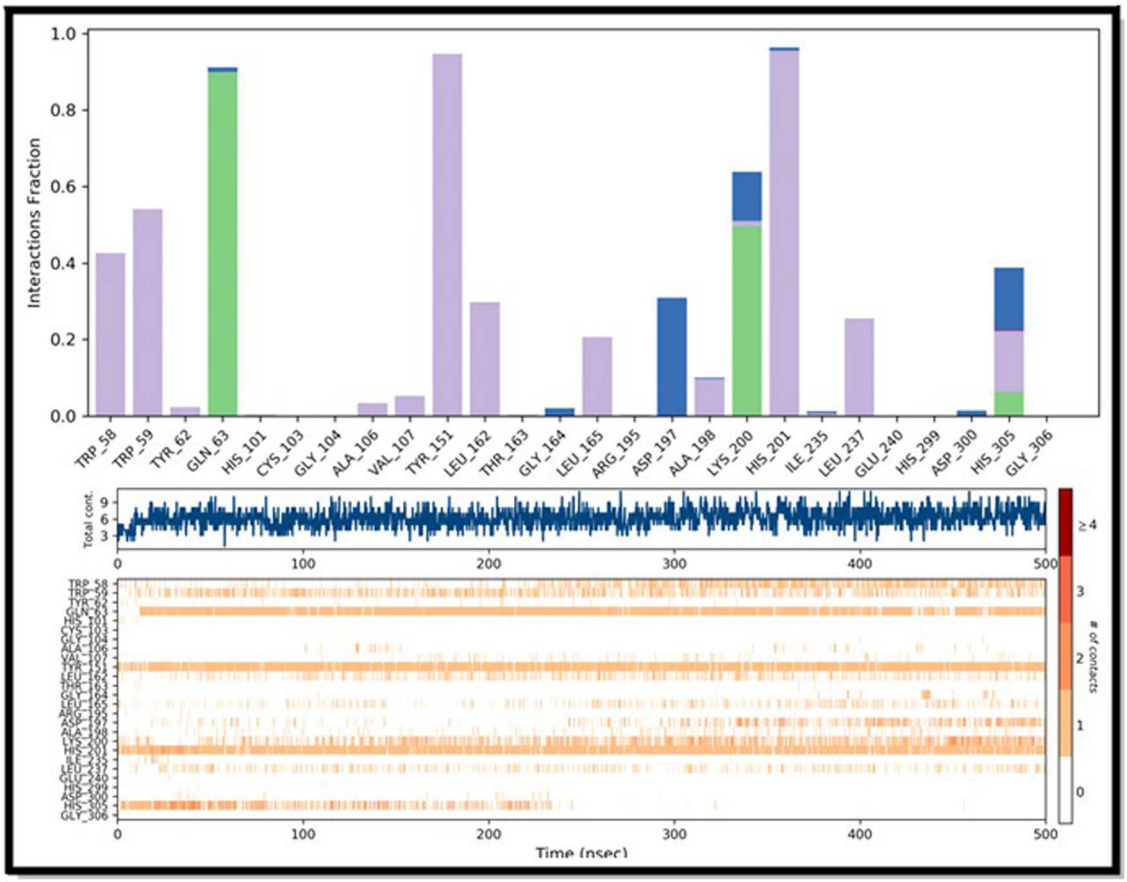

Fig. 15 Interaction analysis of complex **13c** with α-amylase.

noted to be 0.168 eV and 0.158 eV, respectively (Fig. 27). Both compounds have comparable energy gaps, which is vital to estimate the chemical reactivity and polarizability. To get deep insights into the stability of **13c** and **13e**, multiple global descriptors such as softness, electron affinity, chemical potential, electronegativity, *etc.*, were determined from HOMO–LUMO as mentioned in Table 6.

2.8.3 Molecular electrostatic potential analysis of compounds 13c and 13e. MEP analysis of hybrids **13c** and **13e** was conducted to estimate the distribution of charge on the molecular structures. This helps to determine the possible nucleophilic and electrophilic regions (Fig. 28). The yellow and red colors correspond to an electronically rich region, whereas the light blue color represents the electronically poor region. Both compounds **13c** and **13e** possess electronically rich regions around hetero atoms because of their high electronegativity. However, the other areas, such as carbons and hydrogen atoms, act as electrophilic sites due to poor electron density.

2.8.4 NCI analysis of compounds 13c and 13e. The non-covalent interaction (NCI) analysis was carried out to probe weak intra- and intermolecular interactions in compounds **13c** and **13e**. NCI analysis stems from a reduced density gradient that permits grouping and visualization of non-covalent interactions *via* sign(λ_2)ρ *vs.* RDG plots. The negative and positive values of sign(λ_2)ρ represent hydrogen bonding and repulsive attractions, respectively, however, zero value of sign(λ_2)ρ represents weak interactions such as van der Waals. Both compounds **13c** and **13e** demonstrated weak hydrogen bonding (blue color) around hetero atoms. Weak van der Waals interactions (green color) have also been observed between aliphatic parts and aromatic rings. The red regions were also observed due to the presence of bulky groups; however, they did not affect the overall stability of the compounds (Fig. 29).

2.9 α-Amylase inhibition studies

The synthesized piperazine–triazole conjugates **13a–13j** were examined through *in vitro* studies to assess anti-diabetic potential against α-amylase. The results suggested that all compounds exhibited higher potential against α-amylase as compared to the reference compound acarbose (10.30 ± 0.20 μM). Their IC_{50} values fell within the range of 2.39 ± 0.41 μM to 4.54 ± 0.39 μM. It was found that compound **13c** exhibited higher potential among all compounds with an IC_{50} of 2.39 ± 0.41 μM, showing higher potency than the reference compound. Similarly, compound **13e** also displayed significant inhibition with an IC_{50} of 2.97 ± 0.31 μM. In addition, compounds **13b** and **13f** exhibited slightly higher IC_{50} of 4.03 ± 0.28 μM and 4.54 ± 0.39 μM, respectively, as compared to other compounds. Likewise, compounds **13i**, **13j**, **13h**, **13g**, **13a** and **13d** exhibited

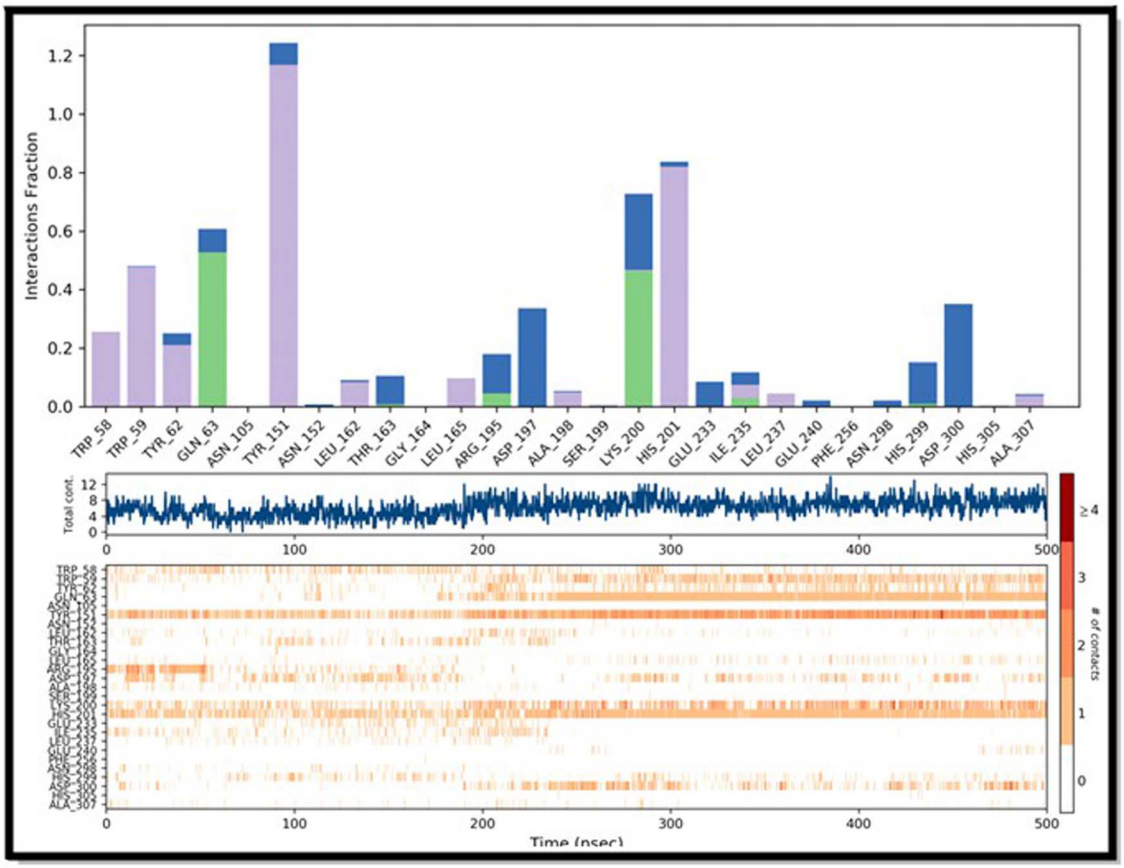

Fig. 16 Interaction analysis of complex **13e** with α-amylase.

strong inhibition against α-amylase with IC_{50} values *i.e.*, 3.47 ± 0.15 μM, 3.03 ± 0.16 μM, 3.09 ± 0.30 μM, 3.76 ± 0.50 μM, 3.14 ± 0.43 μM and 3.55 ± 0.40 μM (Table 7).

2.10 Structure activity relationship

Based on *in vitro* and computational investigation, the SAR studies of piperazine–triazole conjugates were conducted. The synergistic role of all fragments of hybrids **13a–13j**, comprising Boc piperazine, carbonyl, triazole, and substituted benzofurans, contributes to inhibitory activity against α-amylase. It was found that the inhibitory potential of synthesized conjugates appeared to be reliant on the substitution attached to the benzofuran ring. SAR studies revealed that the compound **13c** with Cl substitution on the benzofuran ring has a strong influence on the enzyme inhibition of α-amylase. The presence of an electronegative group on the benzofuran ring gave a binding affinity of −10.5 kcal mol^{-1} and IC_{50} = 2.39 ± 0.41 μM. Likewise, the presence of the methoxy (7-OMe) group on the benzofuran ring of compound **13e** also exerted a strong influence on the inhibition of alpha amylase. The *in vitro* assay revealed an IC_{50} value of 2.97 ± 0.31 μM. Similarly, the *in silico* investigation has also demonstrated similar results, depicting binding affinity of −9.7 kcal mol^{-1} (Fig. 30). It was observed that the compounds with no substitution (**13b** and **13f**) on the benzofuran ring gave less inhibition (IC_{50} = 4.03 ± 0.28 μM

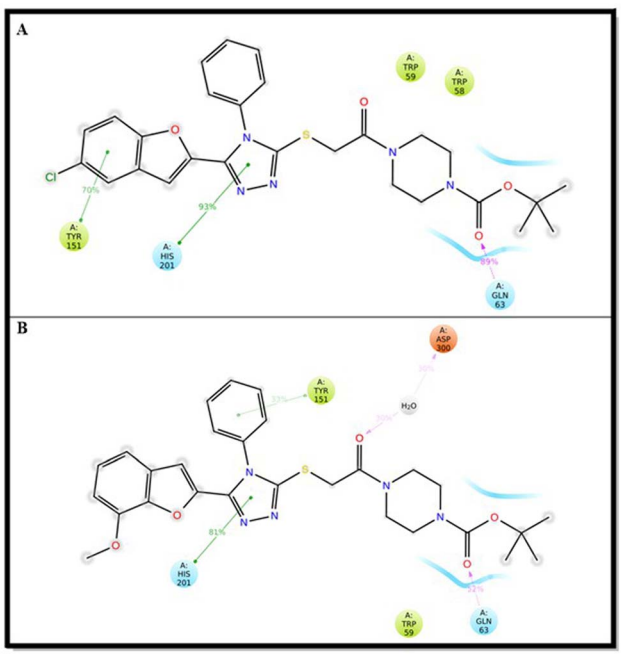

Fig. 17 2D protein–ligand contacts analysis of complex **13c_2QV4** (A) and **13e_2QV4** (B) against α-amylase.

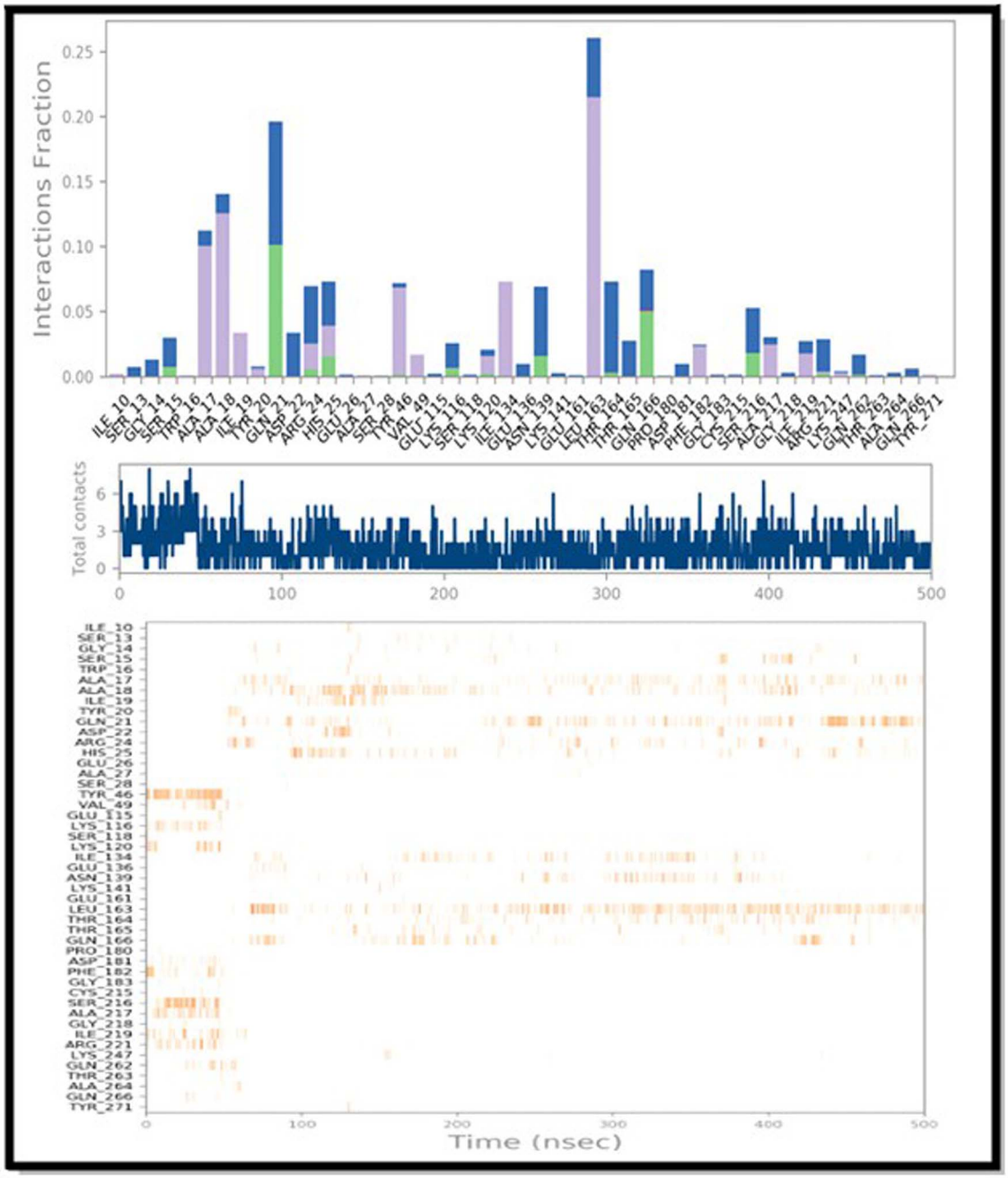

Fig. 18 Time-resolved interaction analysis of complex **13c** with PTP1B.

and 4.54 ± 0.39 μM) as compared with **13c** and **13e**. Likewise, the *in silico* docking affinities of compounds **13b** and **13f** (−8.7 kcal mol^{-1} & −8.5 kcal mol^{-1}) were also found to be less than those of **13c** and **13e**. Additionally, the compounds with **13a**, **13d**, **13g**, **13h**, **13i** and **13j** with ethoxy, 5-Br, diethyl, 6-OMe, 6-Br and 7-Me gave moderate activity in a range from IC_{50} = 3.03 ± 0.16–3.76 ± 0.50 μM and their docking scores were found within −8.8 kcal mol^{-1} to −9.5 kcal mol^{-1} range. However, all the synthesized hybrids exhibited higher activity against the reference compound acarbose (binding affinity = −8.1 kcal mol^{-1} and IC_{50} = 10.30 ± 0.20 μM).

3 Experimental section

3.1 Chemicals and reagents

All solvents and reagents were purchased from Sigma-Aldrich which consumed after purification. WRS-1B melting point apparatus was utilized for observing melting points. ARX FT-NMR spectrometer was used for both ^{13}C NMR spectra (150 MHz) and ^{1}H NMR (600 MHz). The MS spectra were obtained using Agilent 6400 series triple quadrupole mass spectrometer. FTIR specta were recorded using a Cary 630 FTIR spectrometer (Santa Clara, CA, USA).

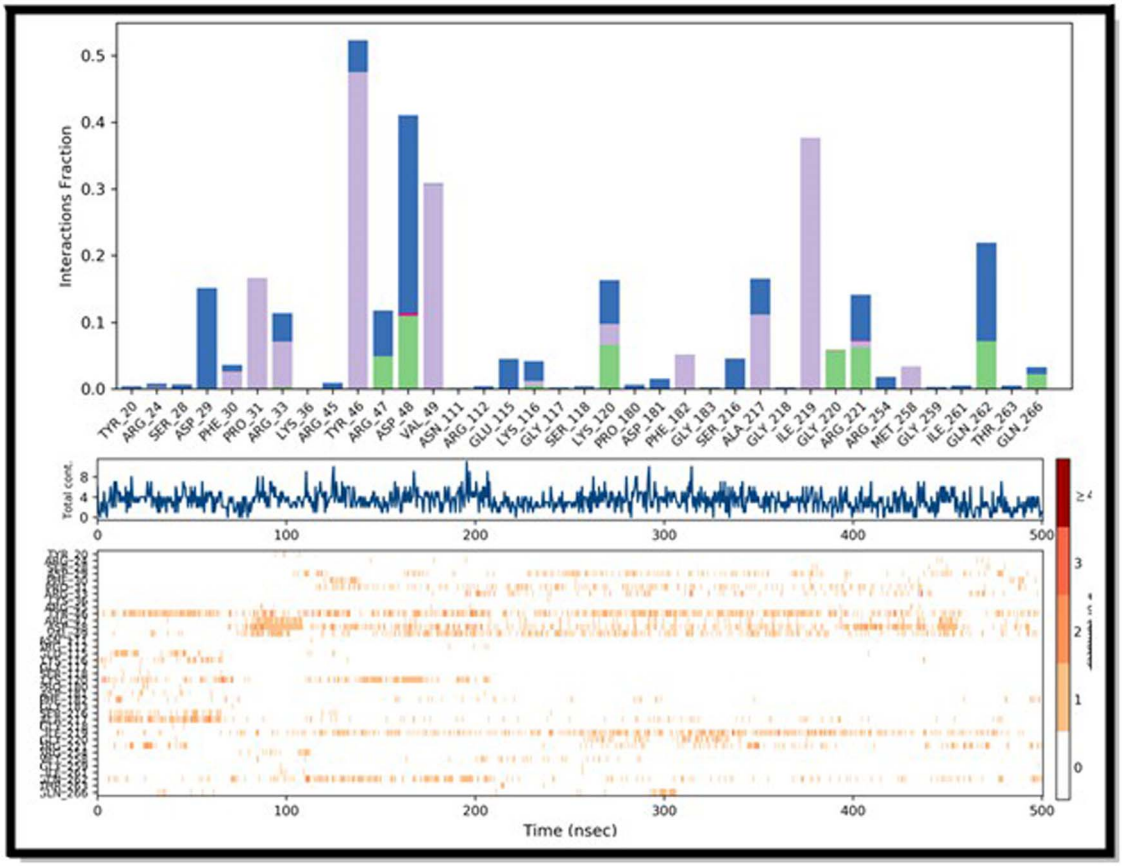

Fig. 19 Time-resolved interaction analysis of complex **13e** with PTP1B.

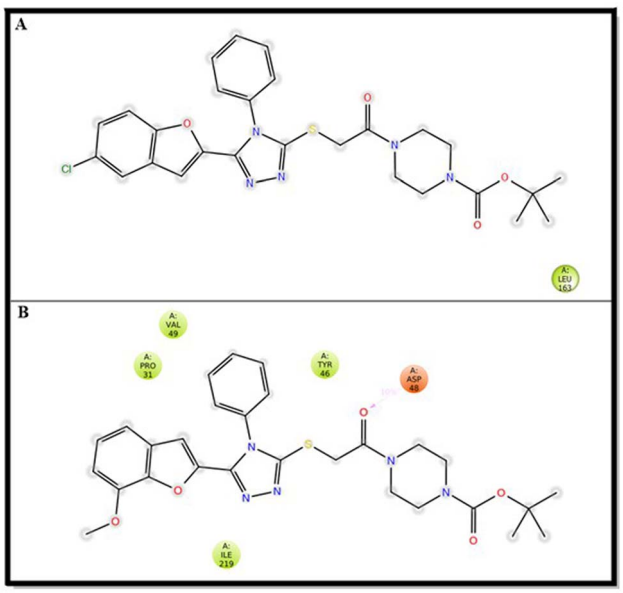

Fig. 20 2D protein–ligand contacts analysis of complex **13c_PTP1B** (A) and **13e_PTP1B** (B).

3.2 Molecular docking and MD protocols

The crystal structures of both PTP1B (PDB: 1NNY) and α-amylase (PDB: 2QV4) was accessed from PDB (protein data bank) web server.[88] The protein structure was prepared in AutoDock tools before performing docking *via* AutoDockVina. The ligand–protein complexes were shifted to Desmond software for MD simulation analysis. The protein was prepared by using protein preparation module of Desmond. Further orthorhombic box, 0.15 NaCl and TIP3P solvent model was used. A 500 ns (2000 frames) simulation were performed using OPLS_2005 force field at 1 atm pressure.[92] Furthermore, MMPBSA analysis was performed by converting trajectories to g_mmpbsa script.

3.3 Enzymatic assay

In order to perform an enzyme inhibition experiment, α-amylase (EC number: 232-588-1, MDL number: MFCD00081319; UNSPSC code: 12352204; eCl@ss: 32160401) was purchased commercially (Sigma-Aldrich) with a concentration of around 30 U/mg sourced out of Aspergillus oryzae. The analytical grade enzyme was used without any additional purification. The soluble starch with a concentration of 1% (w/v) was employed as substrate in enzymatic assay. Acarbose, an α-amylase inhibitor, was characterized well and taken as a reference standard at a concentration of 1 mg mL^{-1}. Inhibition test was performed using 0.1 M phosphate buffer (pH 6.9) according to the methodology described in the literature with slight changes.[93] In short, 100 μL of the test sample was incubated with

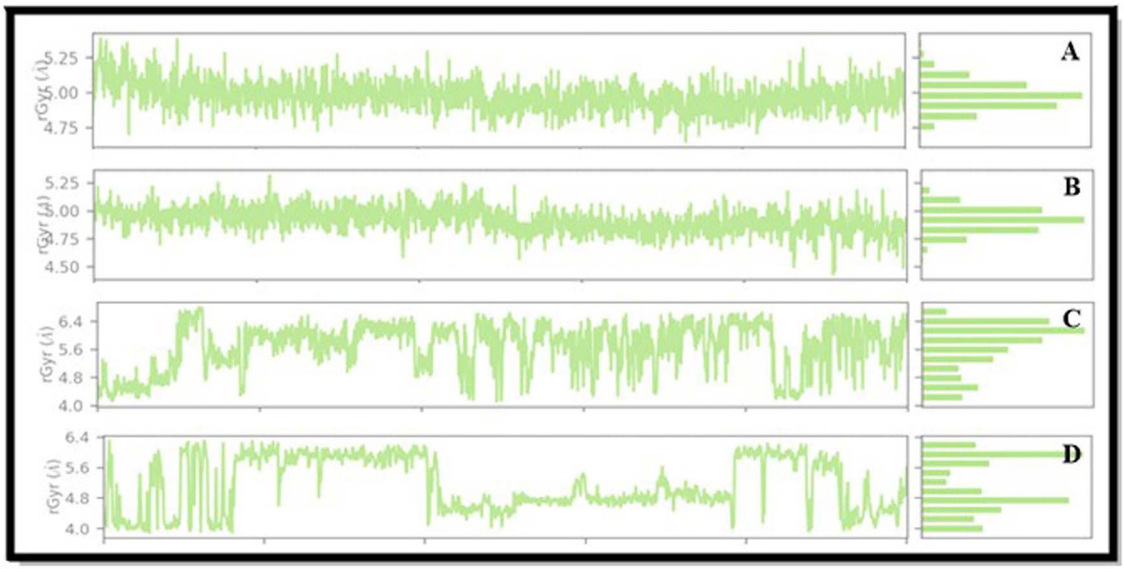

Fig. 21 (A & B) Measurement of rGyr of complex **13c_2QV4** (A) and **13e_2QV4** (B). (C & D) Measurement of rGyr of complex **13c_PTP1B** (A) and 13e_PTP1B.

Table 4 Estimation of binding free energies of target compounds

MMPBSA	13c_2QV4	13e_2QV4	13c_PTP1B	13e_PTP1B
van der Waals energy	−59.12	−53.78	−33.43	−25.39
Electrostatic energy	−11.2	−17.56	−12.48	−1.83
Polar solvation energy	28.21	47.1	28.18	11.22
WCA energy	−1.6	−2.17	−2.96	−0.082
Binding energy	**−43.71**	**−26.41**	**−20.69**	**−16.082**

immobilized enzyme beads (9 U mg) for 15 minutes at 37 °C. Next, 700 μL of 1% soluble starch solution was combined with the mixture and incubated over 5 min at 50 °C. This reaction was stopped by pouring 300 μL DNS reagent and then the mixture was boiled at 100 °C within 5 min. On cooling, 1000 μL of distilled water was added and the absorbance of 540 nm was taken. The rate of percentage inhibition was computed based on the following equation:

$$\% \text{ Inhibition} = (\Delta A \text{ control} - \Delta A \text{ sample})/\Delta A \text{ control} \times 100$$

3.4 Compound and disease targets identification through network pharmacology

The synthesized compounds' targets were identified through the Swiss target prediction web server, followed by the removal of duplicate targets. The visualization of the targets was achieved through Cytoscape software.[94] The therapeutic significance of hyperpigmentation genes was extracted from the GenCard web server using "diabetes" as a keyword. The 33 compound targets were identified through the Swiss target prediction server after taking out replica proteins. Furthermore,

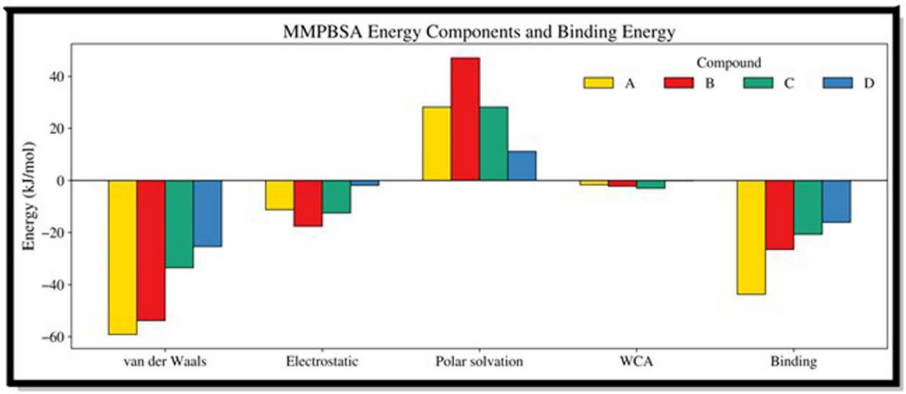

Fig. 22 Representation of individual binding components along with total binding energies of complexes **13c_2QV4** (A), **13e_2QV4** (B), **13c_PTP1B** (C) and **13e_PTP1B** (D).

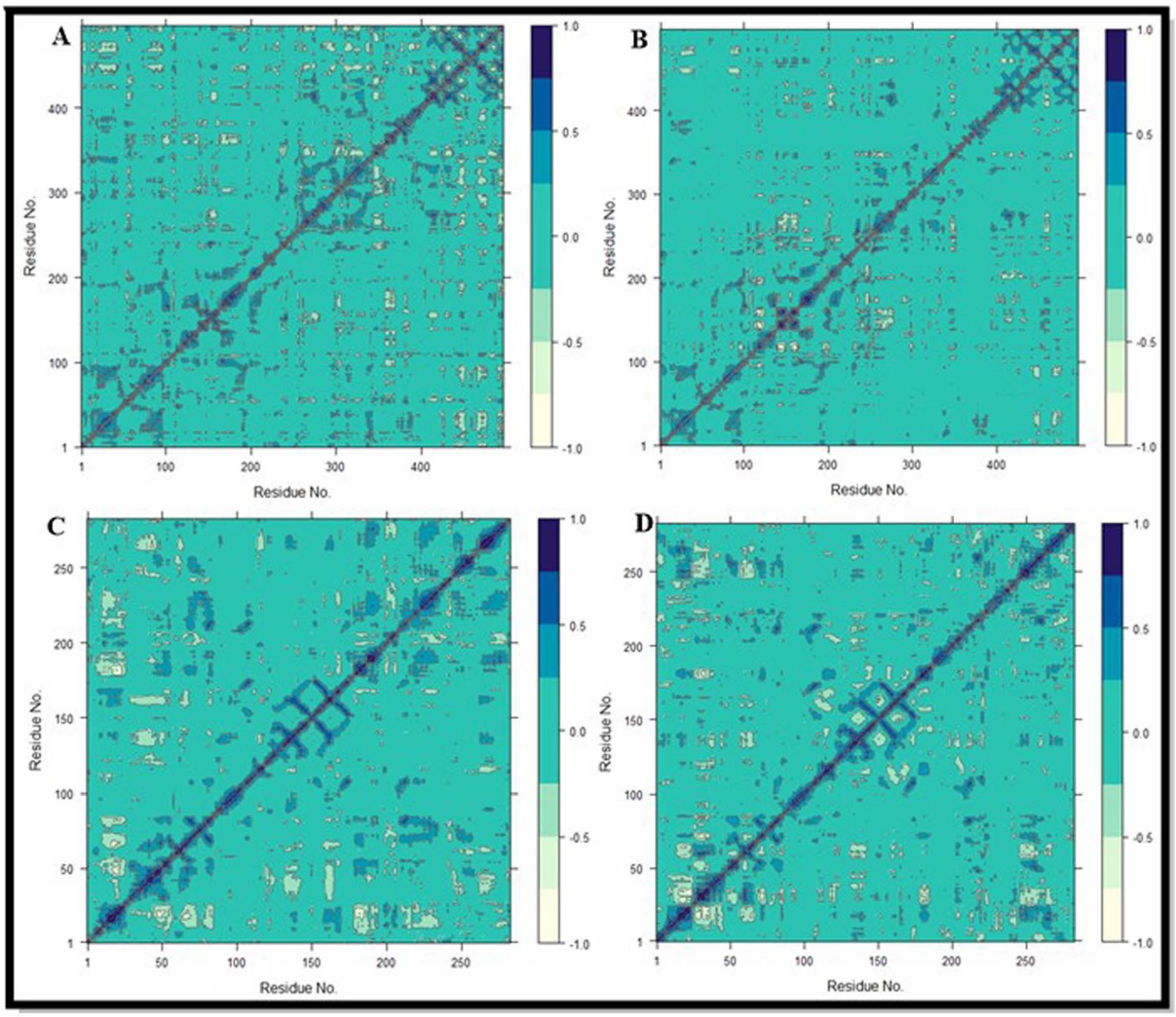

Fig. 23 DCCM analysis of complex **13c_2QV4** (A), **13e_2QV4** (B), **13c_PTP1B** (C) and **13e_PTP1B** (D).

a total of 996 diabetes associated genes were extracted from the GeneCards website using "diabetes" as a keyword. Upon convergence, 43 targets were identified as core genes that might exert therapeutic potential.

3.5 General synthetic procedure

A solution of *tert*-butyl 4-(2-bromoacetyl)piperazine-1-carboxylate **12** (1.1 equivalent) in DCM (5 mL) was allowed to react with substituted benzofuran triazoles **11a–11j** (1 equivalent) in the presence of K_2CO_3 (1.1 equivalent) and KI (0.16 equivalent) for 12–24 hours. The reaction progress was continuously observed *via* TLC. Upon reaction completion, addition of ice-cold water to reaction mixture resulted in the formation of precipitates, which were dried (in an oven) and column chromatography was carried out to obtain the pure products.

3.5.1 Characterization of 13a. Off-white powder; yield 63%; m.p. 139 °C; IR (KBr cm^{-1}): 2974 (C–H), 1669 (C═O, Boc barbonyl), 1636 (C═O, amide), 1559 (C═N), 1499 (C═C, Ar), 1450 (C–H bending), 1363 (CH_3 ending, ^{t}Bu), 1226 (O–Et/C–O), 1161 (C–O), 1122 (C–N), 1073 (C–O), 690 (C–S); ^{1}H NMR (600 MHz, DMSO-d6) $\delta = 1.35$ (t, $J = 6$ Hz, 3H, ethoxy–CH_3), 1.41 (s, 9H, Boc *tert*-butyl), 3.39–3.43 (m, 6H, piperazine–CH_2), 3.48–3.50 (m, 2H, piperazine–CH_2), 4.10 (q, $J = 6$ Hz, 2H, ethoxy–OCH_2–), 4.38 (s, 2H, –S–CH_2–), 6.50 (s, 1H, benzofuran–H), 6.95 (d, $J = 6$ Hz, 1H, benzofuran Ar–H), 7.13–7.15 (m, 2H, benzofuran Ar–H), 7.58 (d, $J = 12$ Hz, 2H, phenyl Ar–H), 7.65–7.69 (m, 3H, phenyl Ar–H); ^{13}C NMR (150 MHz, DMSO-d6) $\delta = 15.2$, 28.5, 28.5, 28.5, 37.1, 41.9, 41.9, 45.7, 45.7, 64.7, 79.7, 107.7, 110.1, 114.3, 128.2, 128.2, 129.2, 129.2, 129.2, 130.7, 131.2, 133.8, 143.2, 143.2, 144.6, 147.5, 152.8, 154.3, 165.8; MS *m*/*z*: 564.1 $[M + 1]^+$; anal. elem. calc. for $C_{29}H_{33}N_5O_5S$: C, 61.79: H, 5.90: N, 12.42: found: C, 61.64: H, 5.89: N, 12.41.

3.5.2 Characterization of 13b. Yellow solid; yield 61%; m.p. 135 °C; IR (KBr cm^{-1}): 2980 (C–H), 1696 (C═O, Boc carbonyl), 1630 (C═O, amide), 1554 (C═N), 1494 (C═C, Ar), 1444 (C–H bending), 1365 (CH_3 bending, ^{t}Bu), 1228 (C–O), 1162 (C–O), 1122 (C–N), 1072 (C–O), 694 (C–S); ^{1}H NMR (600 MHz, DMSO-d6) $\delta = 1.37$ (s, 9H, Boc *tert*-butyl), 3.35–3.39 (m, 6H, piperazine CH_2), 3.44–3.46 (m, 2H, piperazine CH_2), 4.34 (s, 2H, –S–CH_2–), 6.40 (s, 1H, benzofuran H), 7.21 (t, $J = 6$ Hz, 1H,

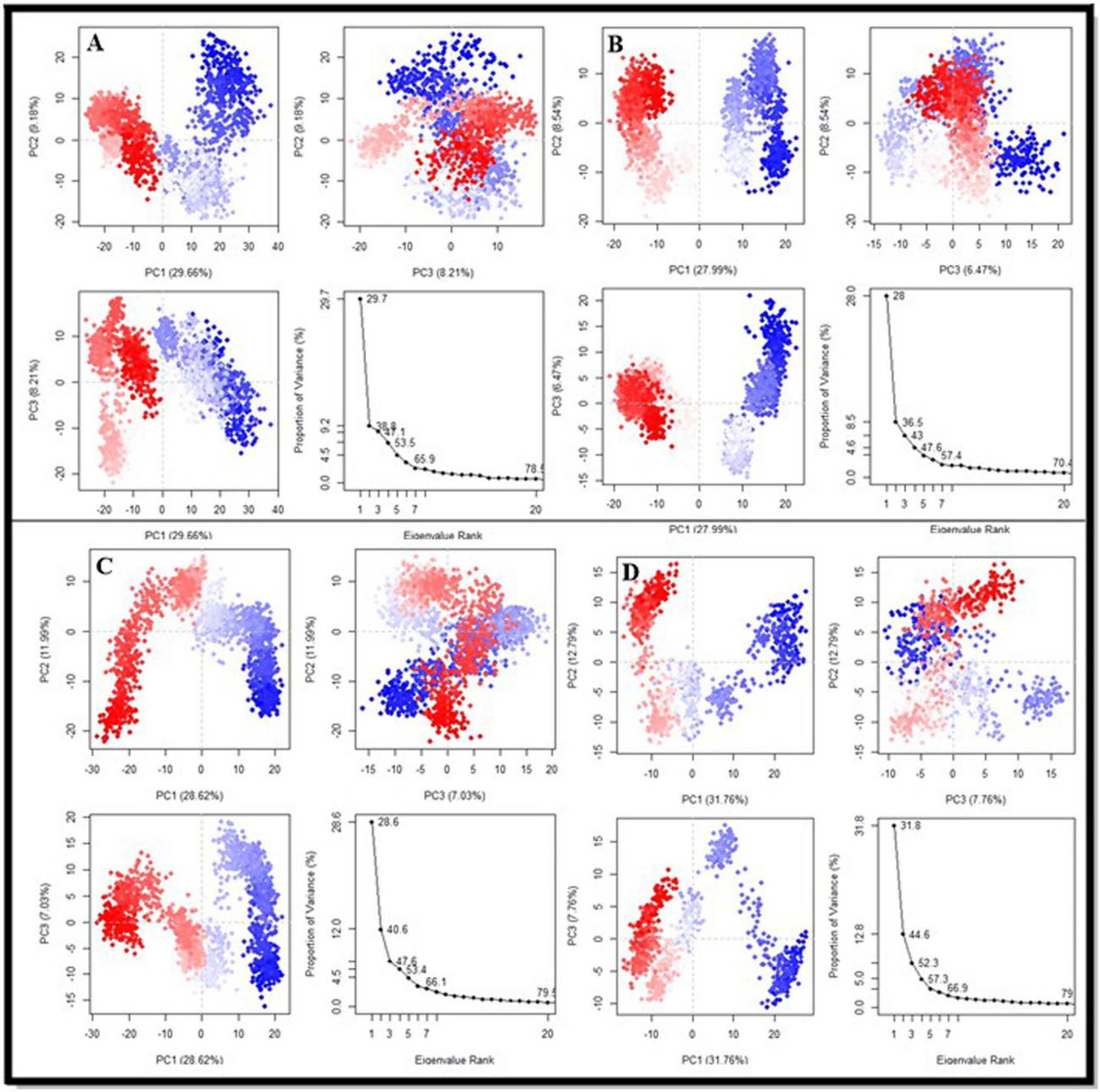

Fig. 24 PCA analysis of complex **13c_2QV4** (A), **13e_2QV4** (B), **13c_PTP1B** (C) and **13e_PTP1B** (D).

benzofuran Ar–H), 7.32 (t, $J = 6$ Hz, 1H, benzofuran Ar–H), 7.52–7.57 (m, 4H, Ar–H (phenyl + benzofuran)), 7.62–7.66 (m, 3H, phenyl Ar–H); ^{13}C NMR (150 MHz, DMSO-d6) δ = 28.5, 28.5, 28.5, 37.1, 41.9, 41.9, 45.7, 45.7, 79.7, 107.4, 111.8, 122.6, 124.2, 126.7, 127.5, 128.2, 128.2, 128.2, 130.7, 131.3, 133.7, 143.2, 147.6, 152.9, 154.3, 154.4, 165.7; MS *m*/*z*: 520 $[M + 1]^+$; anal. elem. calc. for $C_{27}H_{29}N_5O_4S$: C, 62.41: H, 5.63: N, 13.48: found: C, 62.39: H, 5.59: N, 13.49.

3.5.3 Characterization of 13c. Off-white solid; yield 75%; m.p. 148 °C; IR (KBr cm^{-1}): 2974 (C–H), 1700 (C=O, Boc carbonyl), 1633 (C=O, amide), 1560 (C=N), 1493 (C=C, Ar), 1448 (C–H bending), 1362 (CH_3 bending, ^{t}Bu), 1227 (C–O), 1159 (C–O), 1121 (C–N), 1069 (C–O), 690 (C–S); ^{1}H NMR (600 MHz, DMSO-d6) δ = 1.37 (s, 9H, Boc *tert*-butyl), 3.25–3.27 (m, 2H, piperazine CH_2), 3.35–3.39 (m, 4H, piperazine CH_2), 3.44–3.46 (m, 2H, piperazine CH_2), 4.36 (s, 2H, –S–CH_2–), 6.39 (s, 1H, benzofuran H), 7.34–7.36 (m, 1H, benzofuran Ar–H), 7.55–7.59 (m, 3H, Ar–H (phenyl + benzofuran)), 7.63–7.69 (m, 4H, phenyl Ar–H); ^{13}C NMR (150 MHz, DMSO-d6) δ = 28.5, 28.5, 28.5, 37.1, 41.9, 41.9, 45.7, 45.7, 79.7, 106.9, 113.5, 122.0, 126.6, 126.6, 128.1, 128.6, 128.6, 129.2, 130.8, 131.44, 133.6, 144.7, 147.2, 153.0, 153.2, 154.3, 165.7; MS *m*/*z*: 555.9 $[M + 2]^+$; anal. elem. calc. for $C_{27}H_{28}ClN_5O_4S$: C, 58.53: H, 5.09: N, 12.64: found: C, 58.45: H, 5.10: N, 12.61.

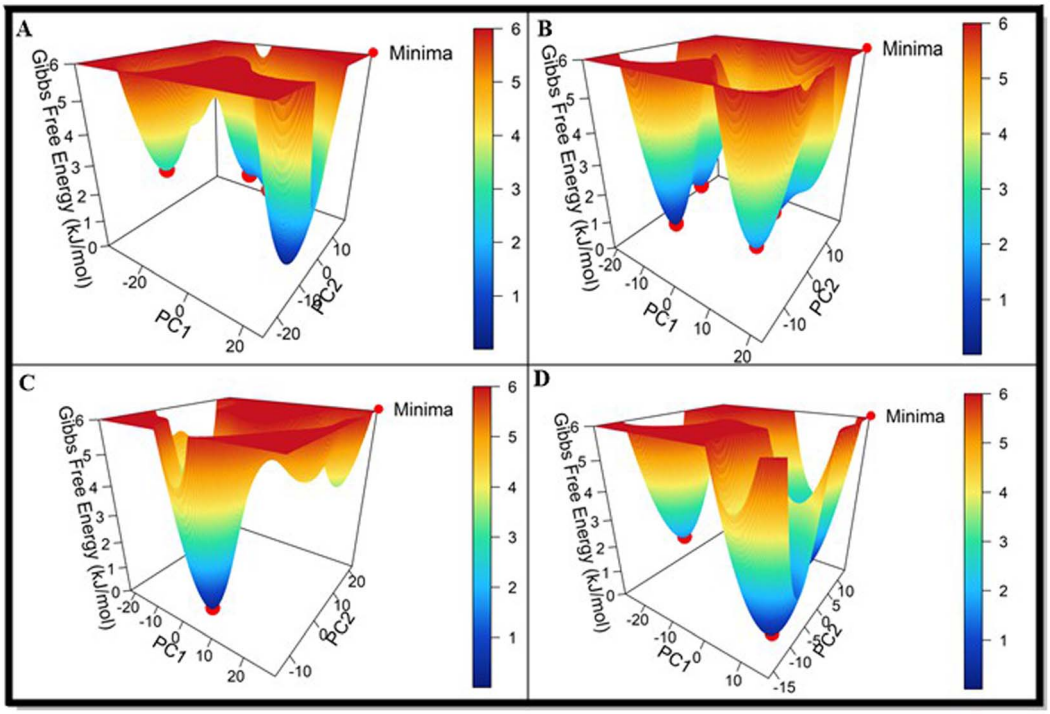

Fig. 25 FEL analysis of complex **13c_2QV4** (A), **13e_2QV4** (B), **13c_PTP1B** (C) and **13e_PTP1B** (D).

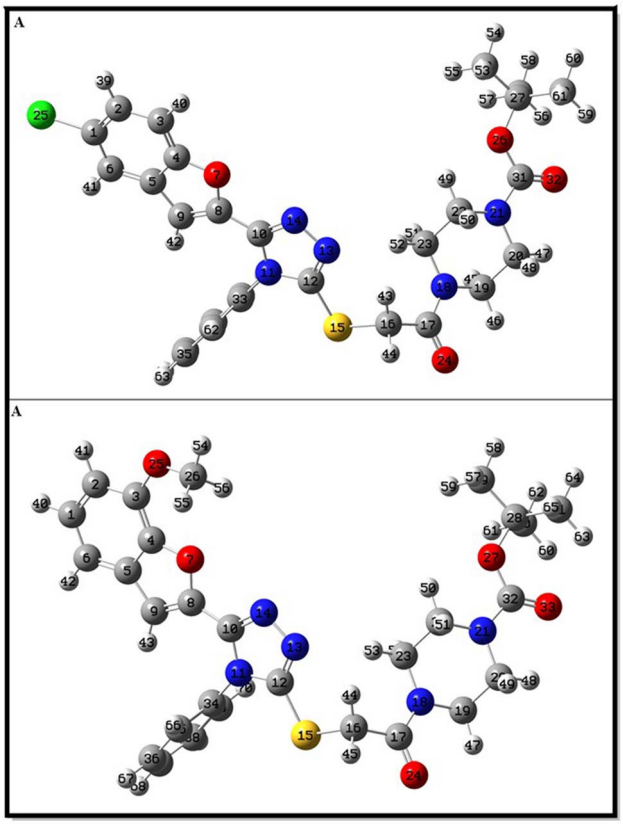

Fig. 26 Geometry optimized structures **13c** (A) and **13e** (B).

3.5.4 Characterization of 13d. Light yellow powder; yield 73%; m.p. 118 °C; IR (KBr cm^{-1}): 2976 (C–H), 1682 (C=O, Boc carbonyl), 1639 (C=O, amide), 1556 (C=N), 1498 (C=C, Ar), 1437 (C–H bending), 1385 (CH_3 bending, ^{t}Bu), 1221 (C–O), 1159 (C–O), 1119 (C–N), 1072 (C–O), 686 (C–S); ^{1}H NMR (600 MHz, DMSO-d6) δ = 1.36 (s, 9H, Boc *tert*-butyl), 3.34–3.38 (m, 6H, piperazine CH_2), 3.43–3.45 (m, 2H, piperazine CH_2), 4.35 (s, 2H, –S–CH_2–), 6.39 (s, 1H, benzofuran H), 7.46 (d, J = 12 Hz, 1H, benzofuran Ar–H), 7.50–7.55 (m, 4H, phenyl Ar–H), 7.59–7.67 (m, 2H, phenyl Ar–H), 7.82 (s, 1H, benzofuran Ar–H), ^{13}C NMR (150 MHz, DMSO-d6) δ = 28.5, 28.5, 28.5, 37.1, 41.9, 41.9, 45.7, 45.7, 79.7, 106.8, 111.6, 113.9, 116.5, 121.2, 124.7, 125.1, 125.1, 128.1, 128.1, 128.1, 129.3, 130.7, 132.5, 148.8, 153.2, 153.2, 165.7; MS m/z: 599.9 $[M + 2]^+$; anal. elem. calc. for $C_{27}H_{28}BrN_5O_4S$: C, 54.18: H, 4.72: N, 11.70: found: C, 54.16: H, 4.69: N, 11.69.

3.5.5 Characterization of 13e. Off-white solid; yield 78%; m.p. 151 °C; IR (KBr cm^{-1}): 2970 (C–H), 1685 (C=O, Boc carbonyl), 1647 (C=O, amide), 1585 (C=N), 1501 (C=C, Ar), 1415 (C–H bending), 1364 (CH_3 bending, ^{t}Bu), 1271 (C–O), 1164 (C–O), 1129 (C–N), 1033 (C–O), 693 (C–S); ^{1}H NMR (600 MHz, DMSO-d6) δ = 1.46 (s, 9H, Boc *tert*-butyl), 3.40–3.42 (m, 2H, piperazine CH_2), 3.50–3.52 (m, 2H, piperazine CH_2), 3.58–3.61 (m, 4H, piperazine CH_2), 3.83 (s, 3H, Ar–OCH_3), 4.35 (s, 2H, –S–CH_2–), 6.56 (s, 1H, benzofuran H), 6.78 (d, J = 6 Hz, 1H, benzofuran H), 7.03–7.11 (m, 2H, benzofuran H), 7.37 (d, J = 12 Hz, 2H, phenyl H), 7.54–7.60 (m, 3H, phenyl H); ^{13}C NMR (150 MHz, DMSO-d6) δ = 28.4, 28.4, 28.4, 36.3, 42.2, 42.2, 46.1, 46.1, 56.5, 80.5, 107.9, 109.1, 113.8, 124.3, 124.3, 127.5, 127.5, 129.2, 130.2, 130.7, 133.3, 142.9, 144.5, 145.6, 148.0, 153.1,

Table 5 Determination of bond lengths and bond angles of geometry optimized structures **13c** & **13e**

Bond lengths (Å)			Bond angles (°)		
Geometry parameters	**13c**	**13e**	Geometry parameters	**13c**	**13e**
C1–C2	1.4	1.4	C2–C1–C6	122.7	121.71
C1–C6	1.38	1.39	C1–C2–C3	120.3	122.06
C2–C3	1.39	1.39	C2–C3–C4	116.76	115.69
C3–C4	1.38	1.4	C3–C4–C5	123.55	122.84
C4–C5	1.4	1.4	C4–C5–C6	119.26	120.24
C5–C6	1.4	1.4	C3–C4–O7	126.01	126.96
C4–O7	1.36	1.37	C4–O7–C8	106.41	106.57
O7–C8	1.37	1.37	O7–C8–C9	111.46	111.29
C8–C9	1.36	1.36	O7–C8–C10	114.63	114.32
C8–C10	1.44	1.44	C8–C10–N11	125.33	125.37
C10–N11	1.39	1.39	C8–C10–N14	124.68	124.68
C10–N14	1.31	1.31	C10–N11–C12	103.88	103.94
N11–C12	1.37	1.37	N11–C12–N13	110.55	110.57
C12–N13	1.31	1.31	N11–C12–S15	121.82	121.66
C12–S15	1.76	1.76	N13–C12–S15	127.62	127.76
S15–C16	1.85	1.85	C12–S15–C16	99.68	99.75
C16–C17	1.53	1.53	S15–C16–C17	111.05	111.06
C17–O24	1.22	1.22	C16–C17–O24	118.41	118.43
C31–C32	1.22	1.22	O24–C17–C18	122.67	122.66

154.5, 165.8; MS *m*/*z*: 550 $[M + 1]^+$; anal. elem. calc. for $C_{28}H_{31}N_5O_5S$: C, 61.19: H, 5.69: N, 12.74: found: C, 61.17: H, 5.63: N, 12.71.

3.5.6 Characterization of 13f. Off-white powder; yield 70%; m.p. 139 °C; IR (KBr cm^{-1}): 2969 (C–H), 1700 (C=O, Boc carbonyl), 1653 (C=O, amide), 1559 (C=N), 1494 (C=C, Ar), 1437 (C–H bending), 1365 (CH_3 bending, ^{t}Bu), 1231 (C–O), 1159 (C–O), 1119 (C–N), 1072 (C–O), 693 (C–S); ^{1}H NMR (600 MHz, DMSO-d6) δ = 1.46 (s, 9H, Boc *tert*-butyl), 3.41–3.62 (m, 8H, piperazine CH_2), 4.37 (s, 2H, –S–CH_2–) 6.92 (s, 1H, benzofuran H), 7.42–7.72 (m, 9H, Ar–H), 7.85–7.89 (m, 2H, naphthyl Ar–H); ^{13}C NMR (150 MHz, DMSO-d6) δ = 28.4, 28.4, 28.4, 38.9, 42.2, 42.2, 46.1, 46.1, 80.5, 106.4, 112.4, 123.0, 123.4, 125.2, 125.2, 126.8, 127.3, 127.3, 127.3, 127.6, 128.9, 128.9, 128.9, 130.3, 130.9, 133.4, 142.2, 148.3, 152.8, 154.5, 165.8; MS *m*/*z*: 570 [*M* +

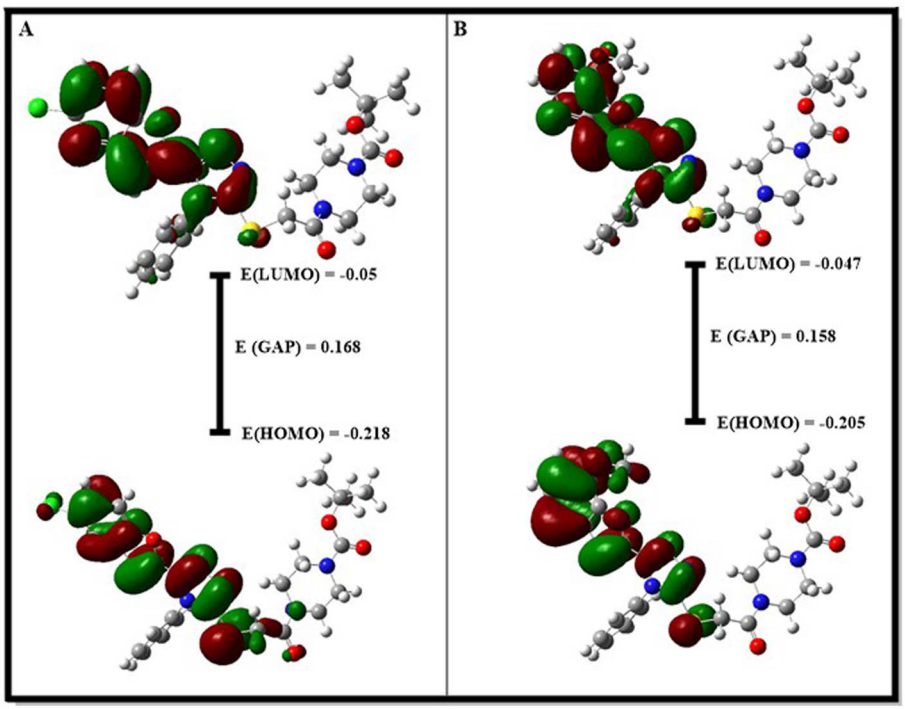

Fig. 27 FMO analysis of compounds **13c** (A) and **13e** (B).

Table 6 Estimation of global descriptors through HOMO–LUMO[a]

Quantum descriptors	13c	13e
HOMO (eV)	−0.218	−0.205
LUMO (eV)	−0.05	−0.047
ΔE (eV)	0.168	0.158
I (eV)	0.218	0.205
A (eV)	0.05	0.047
μ (eV)	−0.134	−0.126
χ (eV)	0.134	0.126
η (eV)	0.084	0.079
σ (eV^{-1})	5.95	6.33
ω (eV)	0.107	0.101

[a] ΔE = energy gap, I = ionization potential, A = electron affinity, μ = chemical potential, χ = electronegativity, η = chemical hardness, σ = softness and ω = electrophilicity index.

1]$^+$; anal. elem. calc. for $C_{31}H_{31}N_5O_4S$: C, 65.36: H, 5.49: N, 12.29: found: C, 65.33: H, 5.45: N, 12.31.

3.5.7 Characterization of 13g. Light yellow solid; yield 67%; m.p. 141 °C; IR (KBr cm^{-1}): 2971 (C–H), 1691 (C=O, Boc carbonyl), 1641 (C=O, amide), 1555 (C=N), 1493 (C=C), 1438 (C–H bending), 1393 (CH_3 bending) 1254 (C–O), 1213 (C–O), 1118 (C–N), 1028 (C–O), 694 (C–S); ^{1}H NMR (600 MHz, DMSO-d6) δ = 1.03 (t, J = 9 Hz, 6H, diethylamino CH_3), 1.37 (s, 9H, Boc *tert*-butyl), 3.25–3.27 (m, 2H, piperazine CH_2), 3.30–3.32 (m, 4H, –NCH_2CH_3), 3.37–3.40 (m, 4H, piperazine CH_2), 3.43–3.45 (m, 2H, piperazine CH_2), 4.29 (s, 2H, –S–CH_2–CO–), 6.05 (s, 1H, benzofuran H), 6.62 (d, J = 6 Hz, 1H, benzofuran Ar–H), 6.67 (s, 1H, benzofuran Ar–H), 7.25 (d, J = 12 Hz, 1H, benzofuran Ar–H), 7.51 (d, J = 6 Hz, 2H, phenyl Ar–H), 7.62–7.65 (m, 3H, phenyl Ar–H); ^{13}C NMR (150 MHz, DMSO-d6) δ = 12.8, 12.8, 28.5, 28.5, 28.5, 37.1, 41.9, 41.9, 44.6, 44.6, 45.7, 45.7, 79.7, 93.1, 107.6, 110.6, 116.1, 122.6, 128.3, 128.3, 128.3, 130.7, 131.2, 133.9, 140.1, 147.7, 148.1, 151.9, 154.3, 157.2, 165.8; MS m/z: 590.9 $[M]^+$; anal. elem. calc. for $C_{31}H_{38}N_6O_4S$: C, 63.03: H, 6.48: N, 14.23: found: C, 63.01: H, 6.42: N, 14.21.

3.5.8 Characterization of 13h. Off-white powder; yield 72%; m.p. 137 °C; IR (KBr cm^{-1}): 2968 (C–H), 1701 (C=O, Boc carbonyl), 1641 (C=O, amide), 1612 (C=N), 1496 (C=C, Ar), 1451 (C–H bending), 1365 (CH_3 bending, ^{t}Bu), 1239 (C–O), 1155 (C–O), 1116 (C–N), 1081 (C–O), 692 (C–S); ^{1}H NMR (600 MHz, DMSO-d6) δ = 1.41 (s, 9H, Boc *tert*-butyl), 3.39–3.43 (m, 6H, piperazine CH_2), 3.47–3.49 (m, 2H, piperazine CH_2), 3.79 (s, 3H, Ar–OCH_3), 4.36 (s, 2H, –S–CH_2–CO–), 6.30 (s, 1H, benzofuran H), 6.87 (d, J = 12 Hz, 1H, benzofuran Ar–H), 7.18 (s, 1H, benzofuran Ar–H), 7.47 (d, J = 6 Hz, 1H, benzofuran Ar–H), 7.58 (d, J = 6 Hz, 2H, phenyl Ar–H), 7.66–7.71 (m, 3H, phenyl Ar–H); ^{13}C NMR (150 MHz, DMSO-d6) δ = 28.5, 28.5, 28.5, 37.1, 41.9, 41.9, 45.7, 45.7, 56.2, 79.7, 96.1, 107.5, 120.6, 122.8, 122.8, 128.2, 128.2, 128.2, 130.8, 131.3, 133.8, 142.3, 147.7, 152.5, 154.3, 155.8, 159.5, 165.8; MS m/z: 550 $[M + 1]^+$; anal. elem. calc. for $C_{28}H_{31}N_5O_5S$: C, 61.19: H, 5.69: N, 12.74: found: C, 61.15: H, 5.58: N, 12.73.

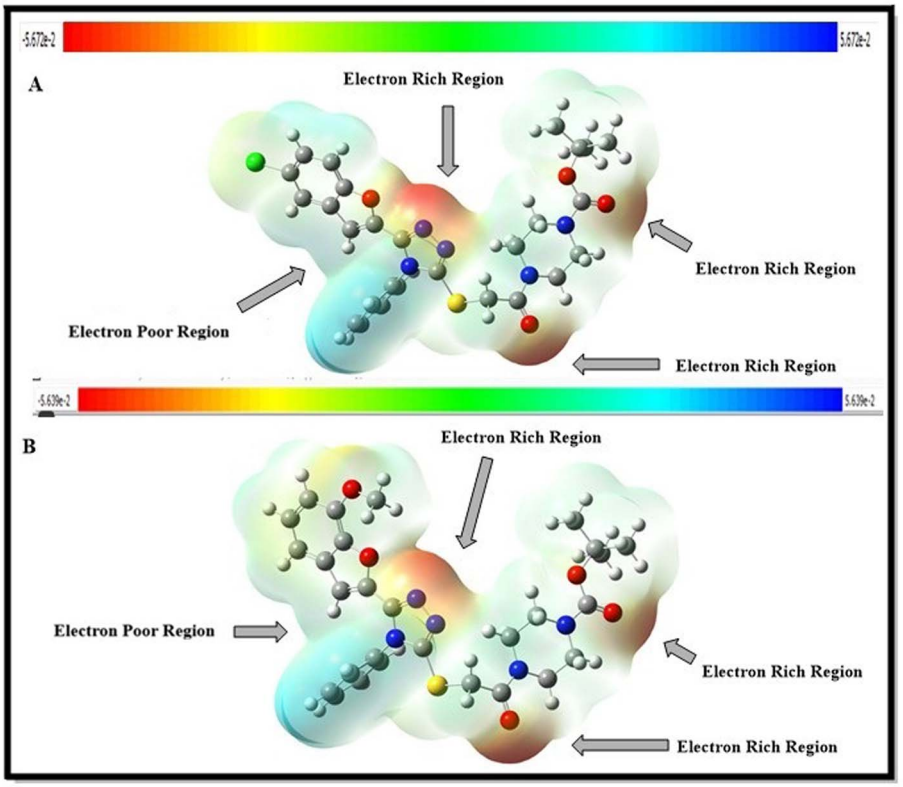

Fig. 28 MEP analysis of compounds 13c (A) and 13e (B).

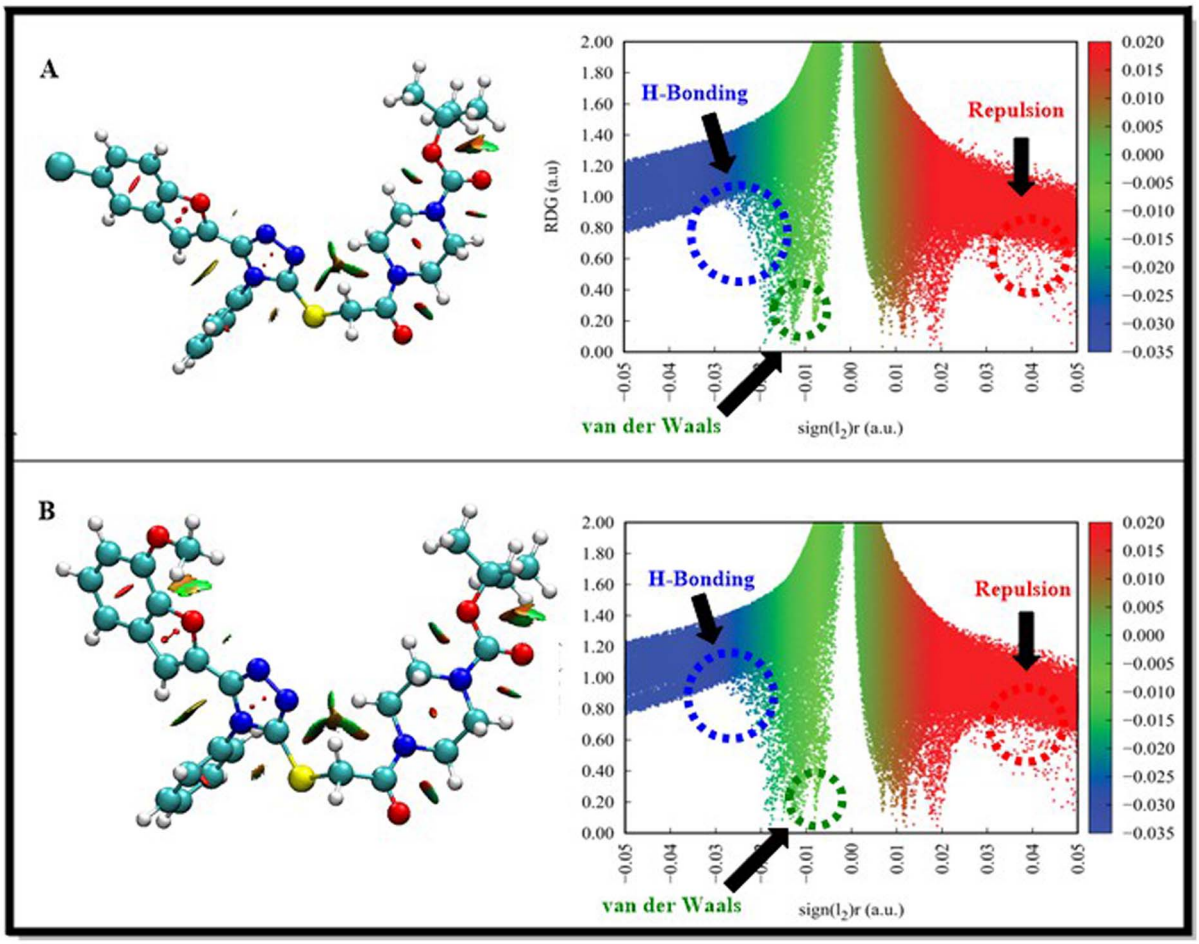

Fig. 29 NCI analysis of compounds **13c** (A) and **13e** (B).

Table 7 α-Amylase inhibition potential of piperazine–triazole conjugates **13a–13j**

Compounds	IC_{50} (μM)
13a	3.14 ± 0.43
13b	4.03 ± 0.28
13c	2.39 ± 0.41
13d	3.55 ± 0.40
13e	2.97 ± 0.31
13f	4.54 ± 0.39
13g	3.76 ± 0.50
13h	3.09 ± 0.30
13i	3.47 ± 0.15
13j	3.03 ± 0.16
Acarbose	10.30 ± 0.20

3.5.9 Characterization of 13i. Off-white solid; yield 68%; m.p. 128 °C; IR (KBr cm^{-1}): 2974 (C–H), 1691 (C=O, Boc carbonyl), 1638 (C=O, amide), 1558 (C=N), 1504 (C=C, Ar), 1446 (C–H bending), 1363 (CH_3 bending, ^{t}Bu), 1234 (C–O), 1168 (C–O), 1119 (C–N), 1081 (C–O), 692 (C–S) ^{1}H NMR (600 MHz, DMSO-d6) δ = 1.41 (s, 9H, Boc *tert*-butyl), 3.39–3.43 (m, 4H, piperazine CH_2), 3.48–3.50 (m, 4H, piperazine CH_2), 4.39 (s, 2H, –S–CH_2–CO–), 6.41 (s, 1H, benzofuran H), 7.43 (d, J = 6 Hz, 1H, benzofuran Ar–H), 7.57–7.61 (m, 3H, phenyl Ar–H), 7.66–7.71 (m, 3H), 7.92 (s, 1H, phenyl Ar–H); ^{13}C NMR (150 MHz, DMSO-d6) δ = 28.5, 28.5, 28.5, 37.1, 41.9, 41.9, 45.7, 45.7, 79.7, 107.3, 115.1, 119.2, 124.1, 126.9, 127.5, 128.1, 128.1, 128.3, 130.8, 131.4, 133.6, 143.9, 147.2, 153.2, 154.3, 154.8, 165.7; MS *m*/*z*: 599.9 $[M + 2]^+$; anal. elem. calc. for $C_{27}H_{28}BrN_5O_4S$: C, 54.18: H, 4.72: N, 11.70: found: C, 54.13: H, 4.71: N, 11.71.

3.5.10 Characterization of 13j. White powder; yield 71%; m.p. 147 °C; IR (KBr cm^{-1}): 2981 (C–H), 1686 (C=O, Boc carbonyl), 1638 (C=O, amide), 1557 (C=N), 1502 (C=C, Ar), 1418 (C–H bending), 1364 (CH_3 bending, ^{t}Bu), 1263 (C–O), 1167 (C–O), 1119 (C–N), 1026 (C–O), 693 (C–S). ^{1}H NMR (600 MHz, DMSO-d6) δ = 1.41 (s, 9H, Boc *tert*-butyl), 2.21 (s, 3H, benzofuran–CH_3), 3.39–3.43 (m, 6H, piperazine CH_2), 3.48–3.50 (m, 2H, piperazine CH_2), 4.36 (s, 2H, –S–CH_2–CO–), 6.83 (s, 1H, benzofuran H), 7.15 (d, J = 6 Hz, 2H, benzofuran Ar–H), 7.44 (t, J = 6 Hz, 1H, benzofuran Ar–H), 7.59 (d, J = 6 Hz, 2H, phenyl Ar–H), 7.63–7.69 (m, 3H, phenyl Ar–H); ^{13}C NMR (150 MHz, DMSO-d6) δ = 14.5, 28.5, 28.5, 28.5, 37.0, 41.9, 41.9, 45.7, 45.7, 79.7, 107.8, 120.0, 121.5, 124.3, 127.0, 127.1, 128.3, 128.3, 128.3, 130.4, 131.0, 134.0, 143.2, 147.7, 152.6, 153.5, 154.3, 165.8; MS

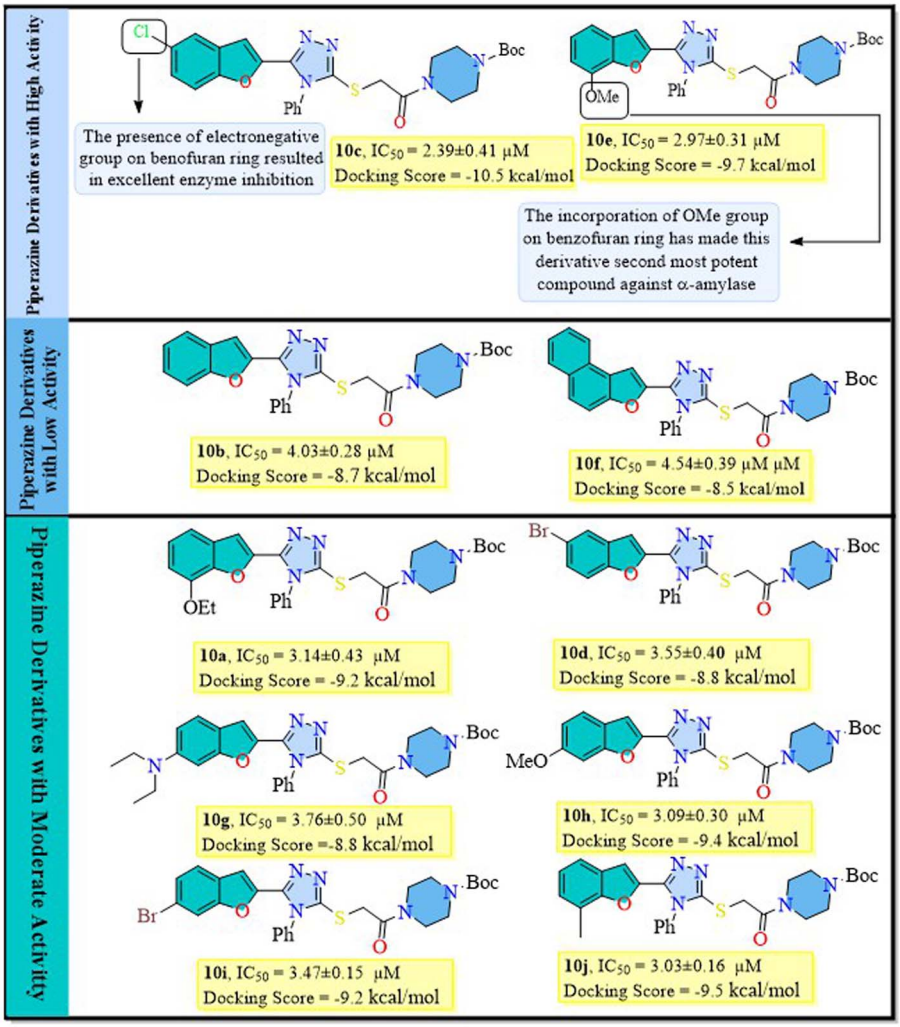

Fig. 30 SAR studies of piperazine derivatives **13a–13j** against α-amylase.

m/*z*: 534.0 $[M + 1]^+$; anal. elem. calc. for $C_{28}H_{31}N_5O_4S$: C, 63.02: H, 5.86: N, 13.12: found: C, 63.05: H, 5.83: N, 13.13.

4 Conclusion

To summarize, a series of piperazine conjugates **13a–13j** was synthesized in moderate to good yields (61–78%). The antidiabetic potential of all derivatives was determined *via in silico* and *in vitro* analysis. The *in vitro* studies identified **13c** and **13e** as potent compounds with lower IC_{50} values *i.e.*, 2.39 ± 0.41 µM and 2.97 ± 0.31 µM against standard acarbose (10.30 ± 0.20 µM). The molecular docking analysis revealed that both **13c** and **13e** were accurately aligned with in the binding pocket of both α-amylase and PTP1B. They were found to be involved in multiple hydrogen bonding and hydrophobic interactions, indicating strong linkage with important amino acids. Furthermore, FMO analysis disclosed that compounds **13c** and **13e** exhibited 0.168 eV and 0.158 eV energy gaps. NCI analysis indicated that both **13c** and **13e** illustrated both H-bonding and van der Waals interactions. The dynamic stability of compounds **13c** and **13e** was assessed *via* MD simulation (rGyr, RMSD, RMSF and protein–ligand contact analysis). Furthermore, binding free energy analysis revealed that both compounds **13c** and **13e** have higher stability within in the binding pocket of PTP1B and α-amylase. Free energy landscape, PCA, and DCCM analysis further validated that **13c** and **13e** have intense global minima and strong correlation within the active site. From these findings, **13c** and **13e** turn out to be effective candidates against diabetes. However, further confirmation *via in vivo* experiments is necessary to validate their effectiveness and safety. Ultimately, these results open a path for the synthesis of anti-diabetic drugs for the treatment of type II diabetes.

Conflicts of interest

The authors have no conflicts of interest for this research work.

Data availability

All data are contained in the manuscript and supplementary information (SI). Supplementary information: ^{13}C NMR and ^{1}H

NMR of synthesized derivatives, along with additonal figures supporting *in silico* studies. See DOI: https://doi.org/10.1039/d6ra00931j.

Acknowledgements

The authors gratefully acknowledge the facilities provided by the Government College University Faisalabad, Pakistan.

References

1 M. Z. Banday, A. S. Sameer and S. Nissar, Pathophysiology of diabetes: An overview, *Avicenna J. Phytomed.*, 2020, **10**, 174–188.
2 S. A. Antar, N. A. Ashour, M. Sharaky, M. Khattab, N. A. Ashour, R. T. Zaid, E. J. Roh, A. Elkamhawy and A. A. Al-Karmalawy, Diabetes mellitus: Classification, mediators, and complications; A gate to identify potential targets for the development of new effective treatments, *Biomed. Pharmacother.*, 2023, **168**, 115734.
3 D. L. Eizirik, L. Pasquali and M. Cnop, Pancreatic β-cells in type 1 and type 2 diabetes mellitus: different pathways to failure, *Nat. Rev. Endocrinol.*, 2020, **16**, 349–362.
4 U. Galicia-Garcia, A. Benito-Vicente, S. Jebari, A. Larrea-Sebal, H. Siddiqi, K. B. Uribe, H. Ostolaza and C. Martín, Pathophysiology of type 2 diabetes mellitus, *Int. J. Mol. Sci.*, 2020, **21**, 6275.
5 M. Sohrabi, M. R. Binaeizadeh, A. Iraji, B. Larijani, M. Saeedi and M. Mahdavi, A review on α-glucosidase inhibitory activity of first row transition metal complexes: a futuristic strategy for treatment of type 2 diabetes, *RSC Adv.*, 2022, **12**, 12011–12052.
6 U. Hossain, A. K. Das, S. Ghosh and P. C. Sil, An overview on the role of bioactive α-glucosidase inhibitors in ameliorating diabetic complications, *Food Chem. Toxicol.*, 2020, **145**, 111738.
7 E. Ferrannini and R. A. DeFronzo, Impact of glucose-lowering drugs on cardiovascular disease in type 2 diabetes, *Eur. Heart J.*, 2015, **36**, 2288–2296.
8 H. Reddy, P. Tejaswini, K. Sandhiya and V. Ambika, A Review on Recent Pharmacotherapeutic Advancements in the Prevention of Diabetes Mellitus Complications, *Asian J. Res. Med. Pharm. Sci.*, 2025, **13**, 69–77.
9 N. Birhanu, G. Mamo, G. S. Shiferaw, D. Gizachew, F. Belayneh and T. Birhanu, Factors affecting diabetes related hospitalization and in-hospital outcomes of adults with diabetes in south Ethiopia: A prospective observational study, *PLoS One*, 2025, **20**, e0330735.
10 A. Bulu and S. Keser, The relationship between pan-immune inflammation value and different stages of diabetic retinopathy in patients with type 2 diabetes mellitus: a prospective cross-sectional study, *BMC Endocr. Disord.*, 2025, **25**, 184.
11 A. E. Peters, M. Nguyen, J. B. Green, E. R. Pearson, J. B. Buse, H. Sourij, A. F. Hernandez, N. Sattar, R. R. Holman and R. J. Mentz, Proteomic pathways across the ejection fraction spectrum in patients with heart failure and diabetes mellitus: an EXSCEL trial substudy, *Sci. Rep.*, 2025, **15**, 30170.
12 K. Moelgg, A. Karisik, L. Scherer, L. Buergi, B. Dejakum, S. Komarek, J. Granna, C. Boehme, R. Pechlaner and T. Toell, Prediabetes and diabetes mellitus type II after ischemic stroke, *Eur. Stroke J.*, 2025, **10**, 822–828.
13 H. Zhang, H. Tang, Y. Gu, Z. Tang, X. Zhao, R. Zhou, P. Huang, R. Zhang and X. Wang, Association between early-stage diabetic nephropathy and the delayed monophasic glucose peak during oral glucose tolerance test in type 2 diabetes mellitus, *J. Diabetes Invest.*, 2025, **16**, 236–245.
14 D. A. Elsayed, W. Shehta, S. El-Kalyoubi, A. Selim, M. G. Assy, O. Metwally, A. A. Al-Kubaisi, S. A. Awad and F. Marzook, Synthesis and radiolabelled evaluation of novel pyrimidine derivatives as dual α-amylase inhibitors and GIT-targeted molecular imaging probe, *RSC Adv.*, 2025, **15**, 29544–29559.
15 K. Kannan and S. Sadhukhan, A multimodal caffeic acid-derived alkyl-amide antidiabetic agent: targeting α-glucosidase, α-amylase, oxidative stress, and protein glycation, *RSC Adv.*, 2025, **15**, 41833–41849.
16 H. Zaman, A. Saeed, H. Ismail, S. Anwaar, M. Latif, M. Z. Hashmi and H. R. El-Seedi, Correction: Novel pyrimidine linked acyl thiourea derivatives as potent α-amylase and proteinase K inhibitors: design, synthesis, molecular docking and ADME studies, *RSC Adv.*, 2025, **15**, 2318.
17 W. Zareen, N. Ahmed, A. M. Khan, S. N. Mali, N. Sadeghian, N. A. Aldawsari, P. Taslimi, A. K. Alanazi, M. Tahir and M. Tasleem, Synthesis, antidiabetic evaluation, and computational modeling of 3-acetyl-8-ethoxy coumarin derived hydrazones and thiosemicarbazones, *RSC Adv.*, 2025, **15**, 39043–39058.
18 A. Kaur, S. Singh, S. Mujwar and T. G. Singh, Molecular Mechanisms Underlying the Therapeutic Potential of Plant-Based α-Amylase Inhibitors for Hyperglycemic Control in Diabetes, *Curr. Diabetes Rev.*, 2025, **21**, e020724231486.
19 S. I. R. Okoduwa, D. H. Mhya, I. Abdulwaliyu, B. E. Igiri, U. J. Okoduwa, D. E. Arthur, A. O. Laleye, G. J. Osang, O. L. Onaleye and E. Nathyns-Pepple, Phytomedicine approach for management of diabetes mellitus: an overview of scientifically confirmed medicinal plants with hypoglycaemic properties and their probable mechanism of action, *Phytochem. Rev.*, 2025, **24**, 1691–1751.
20 H. Wu, X. Liu, S. Xie, J. Zhou, M. G. Corradini, Y. Pan and X. Cui, Inhibitory effects of phenolic compounds from blueberry leaf on α-amylase and α-glucosidase: kinetics, mode of action, and molecular interactions, *J. Sci. Food Agric.*, 2025, **105**, 4524–4536.
21 K. D. Hernández-González, M. A. Vinchira-Lamprea, J. Hernandez-Aranda and J. A. Olivares-Reyes, Resveratrol Impairs Insulin Signaling in Hepatic Cells via Activation of PKC and PTP1B Pathways, *Int. J. Mol. Sci.*, 2025, **26**, 7434.
22 S. Ali, X. Vidal-Gómez, M. Piquet, L. Vergori, G. Simard, S. Dubois, P.-H. Ducluzeau, P. Pomiès, S. Kamli-Salino and M. Delibégovic, Circulating extracellular vesicle-carried

PTP1B and PP2A phosphatases as regulators of insulin resistance, *Diabetologia*, 2025, **68**, 231–242.

23 C. Li, J. Luo, S. Guo, X. Jia, C. Guo, X. Li, Q. Xu and D. Shi, Highly selective protein tyrosine phosphatase inhibitor, 2,2′,3,3′-tetrabromo-4,4′,5,5′-tetrahydroxydiphenylmethane, ameliorates type 2 diabetes mellitus in BKS db mice, *Mol. Pharmaceutics*, 2019, **16**, 1839–1850.

24 Z. Franklin, C. Hull, M. Delibegovic and B. Platt, Pharmacological PTP1B inhibition rescues motor learning, neuroinflammation, and hyperglycaemia in a mouse model of Alzheimer's disease, *Exp. Neurol.*, 2025, **385**, 115115.

25 Y. Liu and F. Gong, Natural Products From Plants Targeting Leptin Resistance for the Future Development of Anti-Obesity Agents, *Phytother. Res.*, 2025, **39**, 1174–1189.

26 Z. Zhang, M. Zeng, P. Guo, Y. Zhang, K. Ye, J. Sun, Y. Wang, F. Chang, X. Zheng and W. Feng, Salvia miltiorrhiza Bge extract ameliorates abnormalities in glycolipid metabolism in db/db mice by regulating tyrosine metabolism through PTP1B/IRS-1/AKT signaling pathway, *J. Ethnopharmacol.*, 2025, **352**, 120236.

27 W. A. Gómez, G. Humeres, C. A. Orozco-Castaño, R. Cannataro, A. M. Muñoz-Contreras, L. M. Gómez-Miranda, J. L. Petro and D. A. Bonilla, Leptin Signaling and Its Relationship with Obesity-induced Insulin Resistance: A Bioinformatics-assisted Review, *Gene Expression*, 2025, **24**, 56–63.

28 E. A. Elmorsy, H. A. Elsisi, A. S. Alkhamiss, N. S. Alsoqih, M. M. Khodeir, A. A. Alsalloom, A. A. Almeman, S. R. Elghandour, E. H. Nadwa and B. E. A. Khaled, Activation of SIRT1 by SRT1720 alleviates dyslipidemia, improves insulin sensitivity and exhibits liver-protective effects in diabetic rats on a high-fat diet: New insights into the SIRT1/Nrf2/NFκB signaling pathway, *Eur. J. Pharm. Sci.*, 2025, **206**, 107002.

29 M. Wang, H. Fu, G. Lv, R. Zhao, W. Cai, X. Pi and Z. Zhang, Structural characterization and hypoglycemic mechanisms of a Hericium coralloides heteropolysaccharide (HCP-2b) via gut microbiota modulation and PI3K/Akt signaling, *Carbohydr. Polym.*, 2026, **378**, 124879.

30 X. Feng, M. Wang, Y. Wang, R. Liang and C. Yan, Associations between environmental glyphosate exposure and glucose homeostasis indices in US general adults: a national population-based cross-sectional study, *Sci. Rep.*, 2025, **15**, 1627.

31 C. Ma, X. Yang, L. Zhang, J. Zhang, Y. Zhang and X. Hu, BRCA1 regulates glucose and lipid metabolism in diabetes mellitus with metabolic dysfunction-associated steatotic liver disease via the PI3K/Akt signaling pathway, *PLoS One*, 2025, **20**, e0318696.

32 M. Aliyari, S. Ghoflchi, S. I. Hashemy, S. F. Hashemi, A. Reihani and H. Hosseini, The PI3K/Akt pathway: a target for curcumin's therapeutic effects, *J. Diabetes Metab. Disord.*, 2025, **24**, 52.

33 Q. Feng, X. Yu, J. Xie, F. Liu, X. Zhang, S. Li, Y. Wang, S. Pan, D. Liu and Z. Liu, Phillygenin improves diabetic nephropathy by inhibiting inflammation and apoptosis via regulating TLR4/MyD88/NF-κB and PI3K/AKT/GSK3β signaling pathways, *Phytomedicine*, 2025, **136**, 156314.

34 F. J. Patiño, J. M. Galindo, A. Jiménez, Y. Alacid, C. R. Mateo, A. M. Sánchez-Migallón, E. Vázquez, S. Merino and M. A. Herrero, Intrinsic fluorescence hydrogels for ON/OFF screening of antidiabetic drugs: assessing α-glucosidase inhibition by acarbose, *J. Mater. Chem. B*, 2025, **13**, 2717–2724.

35 M. M. Sonsalla, R. Babygirija, M. Johnson, S. Cai, M. Cole, C.-Y. Yeh, I. Grunow, Y. Liu, D. Vertein and M. F. Calubag, Acarbose ameliorates Western diet-induced metabolic and cognitive impairments in the 3xTg mouse model of Alzheimer's disease, *GeroScience*, 2025, **47**, 1569–1591.

36 A. S. Adefegha, B. C. Adedayo, I. S. Oyeleye, H. O. Balogun and G. Oboh, Consequence of bitter gourd (momordica charantia) and bitter leaf (vernonia amygdalina) inclusive diets on acarbose treatment in high-fat/streptozotocin model of diabetic rats, *Comp. Clin. Pathol.*, 2025, **34**, 633–644.

37 P. Aneja, R. Guleria and D. P. Dahiya, In vitro characterization and in vivo antidiabetic studies of designed formulations: nanosponges and nanocrystals of voglibose, *Future J. Pharmaceut. Sci.*, 2025, **11**, 1–21.

38 Ö. T. Akarslan, D. E. Kaya, M. B. Dörtbudak, B. Kilinç, İ. Büyüktaşkapulu, F. Göktürk, M. Demircioğlu, A. Er and B. Dik, Multi-target antidiabetic therapy with voglibose, ubiquinone, and tempol: synergistic effects on liver and skeletal muscle in experimental type 2 diabetes, *BMC Pharmacol. Toxicol.*, 2025, **27**, 21.

39 S. Manandhar, P. C. Gurram, A. Govindula, S. P. Kabekkodu and K. S. R. Pai, Voglibose Attenuates Amyloid Beta–Induced Memory Deficits in a Rodent Model: A Potential Alzheimer's Therapy via Wnt Signaling Modulation, *Mol. Neurobiol.*, 2025, **62**, 12184–12204.

40 H.-M. Kim and C.-G. Hyun, Miglitol, an oral antidiabetic drug, downregulates melanogenesis in B16F10 melanoma cells through the PKA, MAPK, and GSK3β/β-Catenin signaling pathways, *Molecules*, 2022, **28**, 115.

41 Y. Li, Y. Du, X. Zhang, Z. Qu, D. Lian, J. Cui and L. Li, The synergistic inhibition of isoginkgetin with miglitol and acarbose on α-glucosidase: Dynamics enzyme changes tracking, *Int. J. Biol. Macromol.*, 2025, **321**, 146103.

42 A. A. Adegboye, K. M. Khan, U. Salar, S. A. Aboaba, Kanwal, S. Chigurupati, I. Fatima, M. Taha, A. Wadood, J. I. Mohammad, H. Khan and S. Perveen, 2-Aryl benzimidazoles: Synthesis, In vitro α-amylase inhibitory activity, and molecular docking study, *Eur. J. Med. Chem.*, 2018, **150**, 248–260.

43 G. Fanelli, E. Raschi, G. Hafez, S. Matura, C. Schiweck, E. Poluzzi and C. Lunghi, The interface of depression and diabetes: treatment considerations, *Transl. Psychiatry*, 2025, **15**, 22.

44 G. Zucca, B. Vigani, C. Valentino, M. Ruggeri, N. Marchesi, A. Pascale, G. Giovilli, L. Malavasi, G. Sandri and S. Rossi, Chondroitin Sulphate-Chitosan Based Nanogels Loaded with Naringenin-β-Cyclodextrin Complex as Potential Tool

for the Treatment of Diabetic Retinopathy: A Formulation Study, *Int. J. Nanomed.*, 2025, **20**, 907–932.

45 F. S. Tokalı, Y. Demir, H. Şenol, Ş. Ateşoğlu, P. Tokalı, F. Çakır and F. Akbaş, Aldose reductase inhibition properties of novel thiazolidin-2, 4-diones: In vitro and in silico approach for the treatment of diabetes-related complications, *J. Mol. Liq.*, 2025, **426**, 127487.

46 Y. Li, D. Xia and W.-C. Yang, Visible-light-driven domino reactions toward nitrogen-containing heterocycles, *Org. Biomol. Chem.*, 2025, **23**, 8641–8655.

47 H. Li, T. Chen, B. Wu, X. Jin, J. Liu and M. Bao, Recent Advances in the Synthesis of Nitrogen-Containing Heterocycles Based on Hydrazine-Directed C–H Bond Activation/Annulation Reactions, *Eur. J. Org Chem.*, 2025, **28**, e202401233.

48 S. Saeed, A. Mansha, A. F. Zahoor, S. Kamal, A. Irfan, J. Javid, S. Anwar, U. Nazeer, M. Haroon and M. A. Bhat, Naphthofuran-triazoles as effective templates for bacterial tyrosinase inhibition: BTEAC catalyzed ultrasound assisted synthesis, in vitro biological evaluation and in silico validation, *J. Mol. Struct.*, 2025, **1327**, 141209.

49 N. Hosseini Nasab, H. Raza, Y. S. Eom, F. H. Shah, J.-H. Kwak and S. J. Kim, Exploring chalcone-sulfonyl piperazine hybrids as anti-diabetes candidates: design, synthesis, biological evaluation, and molecular docking study, *Mol. Diversity*, 2025, **29**, 43–59.

50 M. Ghasemi, M. Mahdavi, M. Dehghan, M. Eftekharian, S. Mojtabavi, M. A. Faramarzi, A. Iraji and A. Al-Harrasi, Substituted piperazine conjugated to quinoline-thiosemicarbazide as potent α-glucosidase inhibitors to target hyperglycemia, *Sci. Rep.*, 2025, **15**, 1871.

51 S. Verma, A. K. Sirbaiya and P. Yadav, Exploring The Therapeutic Potential Of Benzimidazole-Diethylenediamine, Hexahydro-Pyrazine, 1, 4-Diazacyclohexane Conjugates: A Synthetic Approach Towards The Development Of Antidiabetic And Antioxidant Agents, *Diabetes*, 2025, **5**, 6.

52 G. Abbas, M. S. Akhtar, Q. M. Haq, I. S. Al Amri, D. Wang and H. Hussain, Dipeptidyl peptidase IV inhibitors as a potential target for diabetes: Patent review 2019–present, *Expert Opin. Ther. Pat.*, 2025, **35**, 239–250.

53 B. T. Yoosuf, M. Favas Kt, P. Dutta and D. Bansal, Comprehensive safety profile of dipeptidyl peptidase-4 inhibitors: a post-marketing study based on FAERS database using signal detection algorithms, *Expert Opin. Drug Saf.*, 2025, **24**, 1391–1403.

54 A. Khetre and S. Madhusudan, Biological Screening and IC_{50} Determination of Novel DPP-4 Inhibitory Compounds via Fluorescence-Based Assay, *J. Intern. Med. Pharmacol.*, 2025, **2**, 14–19.

55 C. Irajie, A. Fakhrilou, F. Rasekh, M. Ghasemi, S. Hosseini, M. H. Hashempur, P. Taslimi, M. Mahdavi and A. Iraji, Naphthoquinone-triazole hybrids as anti-diabetic agents: An exploration of in silico and in vitro α-glucosidase and α-amylase inhibition, *Lett. Drug Des. Discovery*, 2025, **22**, 100198.

56 İ. Çapan, M. Hawash, M. T. Qaoud and N. Jaradat, Next-Generation Carbazole-Linked 1,2,4-Triazole-Thione Derivatives: Strategic Design, Synthesis, Molecular Docking, and Evaluation of Antidiabetic Potential, *ACS Omega*, 2025, **10**, 848–861.

57 M. Rakse and R. K. Agrawal, Synthesis and ptp1b inhibitory activity of novel benzothiazole and 1, 2, 4-triazole linked acetamido benzoic acid derivatives as antidiabetic activity, *J. Adv. Sci. Res.*, 2021, **12**, 101–111.

58 V. Kumar, M. Nidhar, N. Yadav, M. Sheraj, S. Sura and A. K. Tewari, Unveiling the conformational analysis of N/S-methylene-N/S linked symmetrical scaffolds of 1, 2-pyridazinone and 1, 2, 4-triazinone derivatives: DPP-4 inhibitors, *J. Mol. Struct.*, 2026, **1358**, 145299.

59 W. Xu and C. Kang, Fragment-Based Drug Design: From Then until Now, and Toward the Future, *J. Med. Chem.*, 2025, **68**, 5000–5004.

60 N. R. Khedkar, M. Sindkhedkar and A. Joseph, Fragment-based drug discovery: Small fragments, big impact–Success stories of approved oncology therapeutics, *Bioorg. Chem.*, 2025, **156**, 108197.

61 M. J. Saif, S. Ahmad, A. Mushtaq, S. Munawar, A. F. Zahoor, S. Ettampola, A. Irfan, K. Kotwica-Mojzych, K. Ruszel and M. Mojzych, Ultrasonic-assisted, additive-free Pd-catalyzed Suzuki–Miyaura cross-coupling enabled synthesis of novel arylated benzofuran-triazole hybrids, *Front. Chem.*, 2025, **13**, 1726528.

62 F. Cao, Y.-S. Cheng, L. Yu, Y.-Y. Xu and Y. Wang, Bioinformatics analysis of differentially expressed genes and protein–protein interaction networks associated with functional pathways in Ulcerative Colitis, *Int. Med. J. Exp. Clin. Res.*, 2021, **27**, e927917–927911.

63 J.-M. Lu, Y.-C. Chen, Z.-X. Ao, J. Shen, C.-P. Zeng, X. Lin, L.-P. Peng, R. Zhou, X.-F. Wang and C. Peng, System network analysis of genomics and transcriptomics data identified type 1 diabetes-associated pathway and genes, *Genes Immun.*, 2019, **20**, 500–508.

64 M. Delibegović, S. Dall'Angelo and R. Dekeryte, Protein tyrosine phosphatase 1B in metabolic diseases and drug development, *Nat. Rev. Endocrinol.*, 2024, **20**, 366–378.

65 S. Koren and I. G. Fantus, Inhibition of the protein tyrosine phosphatase PTP1B: potential therapy for obesity, insulin resistance and type-2 diabetes mellitus, *Best Pract. Res., Clin. Endocrinol. Metab.*, 2007, **21**, 621–640.

66 S.-B. Catrina and X. Zheng, Hypoxia and hypoxia-inducible factors in diabetes and its complications, *Diabetologia*, 2021, **64**, 709–716.

67 V. Ngo and M. L. Duennwald, Nrf2 and oxidative stress: a general overview of mechanisms and implications in human disease, *Antioxidants*, 2022, **11**, 2345.

68 A. Yesupatham and R. Saraswathy, Role of oxidative stress in prediabetes development, *Biochem. Biophys. Rep.*, 2025, **43**, 102069.

69 M. H. Rahman, A. Bhusal, W.-H. Lee, I.-K. Lee and K. Suk, Hypothalamic inflammation and malfunctioning glia in the pathophysiology of obesity and diabetes: Translational significance, *Biochem. Pharmacol.*, 2018, **153**, 123–133.

70 A. Read and M. Schröder, The unfolded protein response: an overview, *Biology*, 2021, **10**, 384.
71 C. De Luca and J. M. Olefsky, Inflammation and insulin resistance, *FEBS Lett.*, 2008, **582**, 97–105.
72 L. Chen, C. Chu, J. Lu, X. Kong, T. Huang and Y.-D. Cai, Gene ontology and KEGG pathway enrichment analysis of a drug target-based classification system, *PLoS One*, 2015, **10**, e0126492.
73 J. Sevillano, M. G. Sánchez-Alonso, J. Pizarro-Delgado and M. d. P. Ramos-Álvarez, Role of receptor protein tyrosine phosphatases (RPTPs) in insulin signaling and secretion, *Int. J. Mol. Sci.*, 2021, **22**, 5812.
74 X. Che, R. Zhao, H. Xu, X. Liu, S. Zhao and H. Ma, Differently expressed genes (DEGs) relevant to type 2 diabetes mellitus identification and pathway analysis via integrated bioinformatics analysis, *Int. Med. J. Exp. Clin. Res.*, 2019, **25**, 9237.
75 A. Singh, R. Kukreti, L. Saso and S. Kukreti, Mechanistic insight into oxidative stress-triggered signaling pathways and type 2 diabetes, *Molecules*, 2022, **27**, 950.
76 A. S. Haider, R. Ambatwar and G. L. Khatik, Insights into PTP1B inhibitors as antidiabetic agents: Current research and future perspectives, *Eur. J. Med. Chem.*, 2025, **295**, 117791.
77 L. Xie, S.-Y. Lee, J. N. Andersen, S. Waters, K. Shen, X.-L. Guo, N. P. H. Moller, J. M. Olefsky, D. S. Lawrence and Z.-Y. Zhang, Cellular effects of small molecule PTP1B inhibitors on insulin signaling, *Biochemistry*, 2003, **42**, 12792–12804.
78 H. Nguyen Xuan, D. Dau Xuan and T. Phan Thi, Computational discovery of transforming growth factor-β receptor I inhibitors from the Endophytic Microorganism Natural Product Database via machine learning, molecular docking and steered molecular dynamics, *R. Soc. Open Sci.*, 2026, **13**, 1–14.
79 M. Aziz, S. A. Ejaz, S. Zargar, N. Akhtar, A. T. Aborode, T. A. Wani, G. E.-S. Batiha, F. Siddique, M. Alqarni and A. A. Akintola, Deep learning and structure-based virtual screening for drug discovery against NEK7: a novel target for the treatment of cancer, *Molecules*, 2022, **27**, 4098.
80 S. Basnet, M. P. Ghimire, T. R. Lamichhane, R. Adhikari and A. Adhikari, Identification of potential human pancreatic α-amylase inhibitors from natural products by molecular docking, MM/GBSA calculations, MD simulations, and ADMET analysis, *PLoS One*, 2023, **18**, e0275765.
81 R. P. P. Neves, P. A. Fernandes and M. J. Ramos, Role of enzyme and active site conformational dynamics in the catalysis by α-amylase explored with QM/MM molecular dynamics, *J. Chem. Inf. Model.*, 2022, **62**, 3638–3650.
82 M. Qian, R. Haser, G. Buisson, E. Duee and F. Payan, The active center of a mammalian. alpha.-amylase. Structure of the complex of a pancreatic. alpha.-amylase with a carbohydrate inhibitor refined to 2.2-. ANG. Resolution, *Biochemistry*, 1994, **33**, 6284–6294.
83 A. M. Rodhi, P. G. Yap, O. A. Olalere and C. Y. Gan, Unveiling α-amylase inhibition: A bioinformatics perspective on peptide properties and amino acid contributions, *J. Mol. Struct.*, 2024, **1305**, 137768.
84 G. D. Brayer, Y. Luo and S. G. Withers, The structure of human pancreatic α-amylase at 1.8 Å resolution and comparisons with related enzymes, *Protein Sci.*, 1995, **4**, 1730–1742.
85 W. Li, S. Yang, J. An, M. Wang, H. Li and X. Liu, Statistical characterization of food-derived α-amylase inhibitory peptides: computer simulation and partial least squares regression analysis, *Molecules*, 2024, **29**, 395.
86 P. Sharma, T. Joshi, T. Joshi, S. Chandra and S. Tamta, Molecular dynamics simulation for screening phytochemicals as α-amylase inhibitors from medicinal plants, *J. Biomol. Struct. Dyn.*, 2021, **39**, 6524–6538.
87 K. Tiwari, V. D. Dwivedi and I. P. Tripathi, Computational screening and molecular dynamics simulation of flavonoids from Mentha arvensis as potential alpha-glucosidase inhibitors for type 2 diabetes mellitus, in *Silico Pharmacology*, 2025, vol. 13, p. 185.
88 S. K. Gautam, R. K. Paul, S. Jain, I. Ahmad, A. A. R. Mahmood, H. Patel, P. V. Babu, M. Wahajuddin and K. Raza, Computational Analysis of Balanites aegyptiaca Phytochemicals as Inhibitors of Human Pancreatic α-Amylase, *Chem. Biodiversity*, 2026, **23**, e03133.
89 L. Fang, H. Zhang, W. Cui and M. Ji, Studies of the mechanism of selectivity of protein tyrosine phosphatase 1B (PTP1B) bidentate inhibitors using molecular dynamics simulations and free energy calculations, *J. Chem. Inf. Model.*, 2008, **48**, 2030–2041.
90 V. S. Murthy and V. M. Kulkarni, Molecular modeling of protein tyrosine phosphatase 1B (PTP 1B) inhibitors, *Bioorg. Med. Chem.*, 2002, **10**, 897–906.
91 S. Qian, M. Zhang, Y. He, W. Wang and S. Liu, Recent advances in the development of protein tyrosine phosphatase 1B inhibitors for Type 2 diabetes, *Future Med. Chem.*, 2016, **8**, 1239–1258.
92 Y. Huang, S. Benni, U. P. Yadav, M. A. Babu, A. Verma, T. G. Singh, N. Bansal and Y. Zhang, Deploying the high-throughput virtual screening (HTVS) approach for the identification of new lactate dehydrogenase (LDH) inhibitors with anticancer assets, *Sci. Rep.*, 2026, **16**, 5921.
93 S. Naila, A. Mushtaq and M. Nadia, Phytochemical analysis, antioxidant, acetylcholinesterase, and α-amylase inhibitors from Hippeastrum hybridum extract, *J. Tradit. Chin. Med.*, 2024, **44**, 496.
94 N. Yeung, M. S. Cline, A. Kuchinsky, M. E. Smoot and G. D. Bader, Exploring biological networks with Cytoscape software, *Curr. Protoc. Bioinf.*, 2008, **23**, 8–13.